

DOI: 10.1002/((please add manuscript number))

Article type: Communication

## A **Quasi-Solid-State** Flexible Fiber-shaped Li-CO<sub>2</sub> Battery with Low Overpotential and High Energy Efficiency

Jingwen Zhou, Xuelian Li, Chao Yang, Yinchuan Li, Kunkun Guo, Jianli Cheng\*, Dingwang Yuan, Chenhui Song, Jun Lu\* and Bin Wang\*

J. Zhou, X. Li, Y. Li, C. Song, Prof. J. Cheng, Prof. B. Wang

Institute of Chemical Materials, China Academy of Engineering Physics, Mianyang, Sichuan 621900, P.R. China

Sichuan Research Center of New Materials, Chengdu, Sichuan 610200, P.R. China

E-mail: binwang@caep.cn

C. Yang, Prof. K. Guo, D. Yuan,

College of Materials Science and Engineering, Hunan University, Changsha, Hunan 410082, P.R. China

Dr. J. Lu

Chemical Sciences and Engineering Division, Argonne National Laboratory, Argonne, Illinois 60439, United States

Keywords: **quasi-solid-state**, fiber-shaped, flexible, Li-CO<sub>2</sub> batteries, low overpotential

The rapid development of wearable electronics requires revolution of power accessories on flexibility and energy density. Li-CO<sub>2</sub> battery has recently been proposed as a novel and promising candidate for the next-generation energy storage system. However, the current Li-CO<sub>2</sub> batteries usually suffer from the dilemma of poor stability, low energy efficiency and leakage of liquid electrolyte, and few flexible Li-CO<sub>2</sub> batteries for wearable electronics have been reported so far. Herein, for the first time, we demonstrated a **quasi-solid-state** flexible fiber-shaped Li-CO<sub>2</sub> battery with low overpotential and high energy efficiency by employing ultrafine Mo<sub>2</sub>C nanoparticles anchored on CNT cloth free-standing hybrid film as the cathode. Due to the synergistic effects of CNT substrate and Mo<sub>2</sub>C catalyst, it achieves a low charge potential below 3.4 V, a high energy efficiency of ~80% and can be reversibly discharged and charged for **40** cycles. Experimental results and theoretical simulation show that the intermediate discharge product Li<sub>2</sub>C<sub>2</sub>O<sub>4</sub> stabilized by Mo<sub>2</sub>C *via* coordinative electrons transfer

should be responsible for the reduction of overpotential. The as-fabricated quasi-solid-state flexible fiber-shaped Li-CO<sub>2</sub> battery can also keep working normally even under various deformation conditions, making it great potential of becoming advanced energy accessories for wearable electronics.

With the rapidly increasing interests on wearable electronics over the past decades, the limited energy density and non-deformable configuration of conventional two-dimensional (2D) lithium-ion batteries (LIBs) have already become the dominant obstacles that are hindering the roads of wearable consumer electronics toward ubiquity.<sup>[1-5]</sup> Hence, it is urgent to develop an alternative high-performance flexible energy storage device to break through the inherent restrictions of rigid LIBs.<sup>[6-8]</sup>

Li-CO<sub>2</sub> battery, a newly conceptual metal-gas battery, has been considered as a promising candidate for the next-generation high-performance electrochemical energy storage system recently.<sup>[9,10]</sup> It possesses a high theoretical energy density *via* the 4-electrons transfer reaction ( $4Li^+ + 3CO_2 + 4e^- \rightarrow 2Li_2CO_3 + C$ ,  $E^\circ = 2.80 \text{ V vs. Li}^+/\text{Li}$ ) and provides a novel environmentally-friendly approach to CO<sub>2</sub> fixing which is of great benefit to alleviate global warming.<sup>[11-13]</sup> Interestingly, Li-CO<sub>2</sub> battery is also very attractive to aerospace exploration, for example, it may be a possible energy system for providing electricity on Mars where the atmosphere consists of 96% CO<sub>2</sub> gas.<sup>[14]</sup>

In spite of the aforementioned favorable factors, very few literatures related to flexible Li-CO<sub>2</sub> battery devices for wearable electronics have been reported so far. After systematical investigations, it is found that the main challenges of fabricating high-performance flexible Li-CO<sub>2</sub> battery devices lie in the following three aspects: (1) carbon nanophases (e.g. ketjen black,<sup>[9,10,15]</sup> CNT,<sup>[11,16]</sup> graphene<sup>[17,18]</sup>) which dominate those known Li-CO<sub>2</sub> battery catalysts induce the formation of Li<sub>2</sub>CO<sub>3</sub>, a wide band gap insulator.<sup>[19,20]</sup> It results in a sluggish kinetics for CO<sub>2</sub> evolution so that a high charge potential of 4.2-4.6 V was commonly required to drive

the degradation of  $\text{Li}_2\text{CO}_3$  in most previous Li- $\text{CO}_2$  batteries.<sup>[10,11,17]</sup> Such high potential not only increases the risk of electrolyte decomposition but also accelerates the oxidation of electrodes.<sup>[21,22]</sup> Meanwhile, originated from the incomplete decomposition, more and more solid carbonate species accumulated in the surface of cathode during cycling, leading to a distinct decrease on catalytic performance and even the rapid extension of impedance up to a “sudden death” of the battery.<sup>[20,23,24]</sup> Consequently, the majority of those reported Li- $\text{CO}_2$  batteries showed a negligible reversibility, or a quite limited cycling performance and rate capability with large polarization and low energy efficiency.<sup>[14,24]</sup> (2) Almost all the reported catalysts for Li- $\text{CO}_2$  batteries were solid powders until now.<sup>[11,14,17]</sup> For fabricating Li- $\text{CO}_2$  batteries, these catalysts are inevitable to be connected with current collector (e.g. carbon paper and nickel foam) to constitute a porous gas cathode before assembly. As a result, it caused a fact that Li- $\text{CO}_2$  batteries have been produced in a 2D rigid bulk structure while the total mass of energy storage system has been unnecessarily enlarged as well.<sup>[16,25]</sup> Such planar indeformable power accessories with heavy weight are obviously not adaptable for flexible and wearable electronics.<sup>[6,26]</sup> (3) Compared with traditional 2D counterparts, one-dimensional (1D) flexible fiber-shaped devices have a remarkable advantage on ergonomics that it enables a superior geometrical conformability into irregular epidermal surfaces, like skins of human body.<sup>[27]</sup> Simultaneously, fiber-shaped devices with the abilities to be woven or integrated into fabrics endow energy accessories with a “breathable” feature which greatly benefits the wearing comfort of electronic equipment.<sup>[27,28]</sup> Nevertheless, the commonly used liquid aprotic electrolyte in current Li- $\text{CO}_2$  battery cells is not appropriate to construct 1D fiber-shaped metal-gas battery devices, because of the leakage of liquid electrolyte and flammable properties.<sup>[29,30]</sup> Developing a **quasi-solid-state** Li- $\text{CO}_2$  battery system with fire-proof gel polymer electrolyte (GPE) is quite desirable for wearable electronics at present.<sup>[16,31,32]</sup>

In this work, we report a **quasi-solid-state** flexible fiber-shaped Li- $\text{CO}_2$  battery with low overpotential and high energy efficiency for the first time, in which the ultrafine  $\text{Mo}_2\text{C}$

nanoparticles anchored on CNT cloth free-standing hybrid film (denoted as CC@Mo<sub>2</sub>C NPs) is utilized as the cathode. On one hand, the introduction of GPE not only can prevent the leakage of electrolyte but also suppress the outbreak of a fire caused by short circuit, thus removing a healthy threat to human body and ensuring the safety of battery system. On the other hand, benefit from the unique structure of CC@Mo<sub>2</sub>C NPs, it exhibits a high capacity of 3415  $\mu\text{Ah cm}^{-2}$ , a low charge plateau below 3.4 V, a high energy efficiency of  $\sim 80\%$ , and can be reversibly discharged and charged for 40 cycles. The as-fabricated 1D **quasi-solid-state** fiber-shaped battery also demonstrates excellent adaptability to irregular surface, and its electrochemical properties can be well maintained under different deformation conditions. Moreover, experimental results combined with density functional theory (DFT) study show that the amorphous intermediate discharge product Li<sub>2</sub>C<sub>2</sub>O<sub>4</sub> can be stabilized by delocalized electrons originated from low-valent Mo atoms in Mo<sub>2</sub>C through the bridge of Mo-O coupling. The thermodynamically unstable Li<sub>2</sub>C<sub>2</sub>O<sub>4</sub> is easier to be decomposed and hence reduces the overpotential of this **quasi-solid-state** fiber-shaped Li-CO<sub>2</sub> battery.

The fabrication procedure of CC@Mo<sub>2</sub>C NPs and the subsequent assembly of **quasi-solid-state** flexible fiber-shaped Li-CO<sub>2</sub> battery are schematically depicted in **Figure 1a**, with the preparation details described in Experimental Section (Supporting Information). From the X-ray diffraction (XRD) patterns of Figure S1, besides the moderate peaks at  $\sim 26^\circ$  ascribed to graphitic carbon, other sharp diffraction peaks agree well with the standard  $\beta$ -Mo<sub>2</sub>C planes (JCPDS card No. 65-8766), which implies the fully phase conversion of Mo<sub>2</sub>C from low-crystalline MoO<sub>2</sub> in CNT cloth (CC@LC-Mo<sub>2</sub>C, Figure S2).<sup>[33-36]</sup> According to the thermal gravimetric analysis (TGA) curve **and XRD pattern** presented in Figure S3a,b, the content of active Mo<sub>2</sub>C in the composite is calculated to be approximately 39.3%. The remaining 60.7% CNTs are considered to play a vital role of substrate in maintaining the mechanical strength of the free-standing hybrid film.

As can be seen from the scanning electron microscopy (SEM) images of CC@Mo<sub>2</sub>C NPs, numerous CNTs loaded with Mo<sub>2</sub>C nanoparticles entangle with each other, forming a highly interconnected three-dimensional (3D) porous network with submicrometer-sized macropores (Figure 1b). The inside optical image illustrates its high flexibility and decent mechanical strength that are indispensable for the subsequent construction of fiber-shaped energy storage device. When examined the hybrid film more carefully (Figure 1c and Figure S5a,b), it is found that ultrafine Mo<sub>2</sub>C nanoparticles with an average diameter of 10~20 nm are homogeneously dispersed on CNTs without any obvious agglomeration, indicating that this *in-situ* conversion strategy can effectively suppress the growth of Mo<sub>2</sub>C particles by location confinement of precursor MoO<sub>2</sub> (Figure S4a,b). Furthermore, according to transmission electron microscopy (TEM) images, it can clearly recognize an interconnected 3D porous network comprising bunches of 1D CNT/Mo<sub>2</sub>C composite (Figure 1d) where quite a few small-sized nanoparticles (< 20 nm) are evenly lied on the CNT framework (Figure 1e and Figure S5c,d), well consistent with the above SEM observation. The selected areas electrons diffraction (SAED) pattern inside also verifies the hybridization of CNT and Mo<sub>2</sub>C. In comparison, no nanoparticles can be found in pristine CNT cloth (Figure S7). The high-resolution TEM (HRTEM) image in Figure 1f shows that highly crystalline Mo<sub>2</sub>C nanoparticles are embedded in the walls of CNTs. The atoms in the high-contrast area exhibit typical hexagonal arrangement with the distance of adjacent lattice being 0.23 and 0.15 nm, in good accordance with the (101) and (110) planes of standard  $\beta$ -Mo<sub>2</sub>C, respectively.<sup>[37,38]</sup> The even distribution of Mo<sub>2</sub>C in 3D porous CNTs substrate is further confirmed by energy dispersive spectrum (EDS) element mappings shown in Figure S6 and scanning transmission electron microscopy (STEM) image together with element mappings of Mo and C presented in Figure 1g-i. Furthermore, it is worthy of noting that even if the CC@Mo<sub>2</sub>C NPs have to tolerate drastic sonication for over 24 h during the preparation of TEM samples, Mo<sub>2</sub>C nanoparticles are still firmly pinned on the CNTs, indicating a robust interfacial bonding between CNT and Mo<sub>2</sub>C. It is believed that such intimate

contact is beneficial for sustaining the structural integrity as well as facilitating the fast and stable transportation of electrons across the interface.

When evaluated as **quasi-solid-state** Li-CO<sub>2</sub> battery cathodes, CC@Mo<sub>2</sub>C NPs flexible free-standing film demonstrates an excellent electrochemical performance. The obvious distinction on cyclic voltammetry curves (CVs) in Figure S8 suggests that CC@Mo<sub>2</sub>C NPs have stronger capability of CO<sub>2</sub> fixation and evolution than those of pure CNTs owing to the introduction of Mo<sub>2</sub>C nanoparticles with high catalytic activity. Then, according to the galvanostatic charge profile displayed in Figure S9, the charge potential of CC@Mo<sub>2</sub>C NPs electrode is stipulated below 4.0 V to make sure the electrode structure integrity.<sup>[24]</sup> Over the potential window of 1.8-4.0 V, the CC@Mo<sub>2</sub>C NPs can deliver a large initial discharge area specific capacity as high as 3415  $\mu\text{Ah cm}^{-2}$  and a reversible capacity of nearly 1000  $\mu\text{Ah cm}^{-2}$  at a current density of 50  $\mu\text{A cm}^{-2}$  **under CO<sub>2</sub>** (**Figure 2a**). It needs to be emphasized that the overwhelming reversible capacity was recorded around 3.55 V during the charge process. We believe that the reversible capacity should be derived from the decomposition of a certain Mo<sub>2</sub>C catalyzed discharged product with higher activity than that of Li<sub>2</sub>CO<sub>3</sub>, because no reversible capacity is observed below 4.2 V for individual CNTs, of which the discharge product Li<sub>2</sub>CO<sub>3</sub> is already confirmed by experiments. **In contrast, the discharge voltages of both CC@Mo<sub>2</sub>C NPs and CNT cloth were rapidly declined to 1.8 V without any recognizable plateau under inert atmosphere of Ar (Figure S10), indicating that the aforementioned electrochemical performance did come from the reduction of CO<sub>2</sub>.** To better depict the advantage on decreasing overpotential, the comparison of galvanostatic discharge/charge curves between CC@Mo<sub>2</sub>C NPs and CNT cloth electrodes was illustrated in Figure 2b. It is explicit that CNT cloth has exposed a large charge/discharge potential difference of 1.87 V, which is approximately 3 times as much as that of CC@Mo<sub>2</sub>C NPs (~0.65 V). **Moreover, this free-standing CNT/Mo<sub>2</sub>C hybrid cathode shows a good cycle stability as well, which can be reversibly discharged and charged for 20 cycles at a lower current density of 20  $\mu\text{A cm}^{-2}$  with a curtailing capacity of 100  $\mu\text{Ah}$**

$\text{cm}^{-2}$  (Figure 2c), and can also last for 40 cycles at relatively higher  $80 \mu\text{A cm}^{-2}$  with  $80 \mu\text{Ah cm}^{-2}$  (Figure S11). When the current densities increased from 20 to 40, 80 and  $100 \mu\text{A cm}^{-2}$ , some acceptable polarizations have appeared and the CC@Mo<sub>2</sub>C NPs electrode can steadily last for 3 cycles at every diverse current density (see Figure S12). After the current density went back to  $20 \mu\text{A cm}^{-2}$ , the discharge plateau of CC@Mo<sub>2</sub>C NPs reverted to 2.8 V again, implying that its chemical activity can be still retained even suffering the serious impact of current at high rate. However, pristine CNT cloth, as the control sample, revealed a quite inferior rate capability, while serious polarizations emerged as the current density increased, as shown in Figure S13.

The reduction of overpotential means less electrical power has to be sacrificed during the round-trip energy storage and release processes, which is of great significance in saving resource and boosting the sustainable development.<sup>[21,24,25]</sup> From Figure 2e, it is obvious that CC@Mo<sub>2</sub>C NPs deliver a median discharge voltage of 2.68 V and a charge voltage of 3.39 V at the first cycle, thus leading to a satisfying energy efficiency of ~80%. Despite that the charge voltages have a slightly shift to around 3.5 V in subsequent cycles, the average energy efficiency is maintained at 75% (Figure 2e). However, pure carbon nanophases like Ketjen Black, CNT and graphene commonly exhibit the energy efficiencies ranging from 60 % to 65% using liquid electrolyte.<sup>[11,15,17]</sup> If the safer quasi-solid-state polymer electrolyte was used in Li-CO<sub>2</sub> battery, the energy efficiency has already proved to be further decreased.<sup>[16,31]</sup> For example, only 58% is recorded in our control sample, pristine CNT cloth (Figure 2d). In addition, the voltage-time curves elucidated in Figure S14 indicate that CC@Mo<sub>2</sub>C NPs based solid-state Li-CO<sub>2</sub> battery can steadily work for over 200 h, during which the overpotential still keeps nearly one-half that of individual CNTs. Moreover, another CNT/Mo<sub>2</sub>C hybrid film with abundant Mo<sub>2</sub>C particles inside (denoted as CC@ab-Mo<sub>2</sub>C NPs) has been synthesized to explore whether the content of Mo<sub>2</sub>C affects the electrochemical performance of these Li-CO<sub>2</sub> batteries (Figure S15). When the proportion of Mo<sub>2</sub>C reaches 85%wt, obvious agglomeration of nanoparticles is observed,

causing CC@ab-Mo<sub>2</sub>C NPs to suffer from a faster polarization, distinct catalytic activity decay and relatively lower energy efficiency, in spite of the larger discharge and reversible capacity. It is also noteworthy that the hybrid film would gradually lose its mechanical strength as the increment of Mo<sub>2</sub>C. The above phenomenon further highlights the important role of nanostructure engineering in facilitating reaction kinetics and maintaining catalytic activity. Subsequently, Figure 2f compares CC@Mo<sub>2</sub>C NPs with some typical reported Li-CO<sub>2</sub> battery cathode materials in terms of various electrochemical properties. It is found that high specific capacity and low charge plateau have both been integrated into this CC@Mo<sub>2</sub>C NPs hybrid film and its energy efficiency outperforms that of all previous catalysts for Li-CO<sub>2</sub> batteries ever reported.<sup>[9,10,15,17,18,21,24,25,31]</sup> The excellent electrochemical performance of CC@Mo<sub>2</sub>C NPs should be attributed to the significant advantages of this unique 0D/1D hybrid nanostructure as follows: Firstly, 3D porous framework entangled by 1D CNTs supplies enough inner space for the deposition of discharge product, and thus opening more active sites to Li<sup>+</sup> and CO<sub>2</sub> gas instead of the electrode surface alone. Secondly, CNT cloth not only serves as the flexible substrate to ensure enough mechanical strength but also provides a conductive network to promote the fast transportation of electrons. Thirdly, those ultrafine Mo<sub>2</sub>C nanoparticles that are highly dispersed on CNTs can act as efficient catalytic sites for both CO<sub>2</sub> reduction reaction (CO<sub>2</sub>RR) and evolution reaction (CO<sub>2</sub>ER), significantly facilitating the reaction kinetics.

Based on the decent mechanical strength and electrochemical performance, CC@Mo<sub>2</sub>C NPs were then employed to fabricate quasi-solid-state flexible fiber-shaped Li-CO<sub>2</sub> battery with low overpotential and high energy efficiency, as a proof-of-concept. The whole energy density of the fabricated Li-CO<sub>2</sub> battery (with a linear density of 70 mg cm<sup>-1</sup>) is estimated to be 117 Wh kg<sup>-1</sup>, which is nearly 400 times of a fiber-shaped Li-ion battery,<sup>[39]</sup> 7.8 times that of a fiber-shaped Al-air battery,<sup>[28]</sup> 1.5 times that of a fiber-shaped Li-air battery<sup>[6]</sup> and so on (see more details in Figure S16 and Table S1), but approximately 1/4 that of a planar Li-CO<sub>2</sub> battery operating at 55 °C.<sup>[16]</sup> The corresponding area and volumetric energy densities of the whole

battery were also given for reference ( $82 \text{ Wh cm}^{-2}$  and  $70 \text{ Wh L}^{-1}$ ). The energy density can be increasingly improved by optimizing the assembly process. More importantly, from **Figure 3a**, it can be observed that this fiber-shaped battery can favourably fit into the irregular surface of a toy and lighten up three high-power light emitting diodes (LEDs) with the total rated power of 0.6 W, indicating a promising perspective toward practical application. Meanwhile, the Li-CO<sub>2</sub> battery device showed high flexibility, which can keep working normally even under the continuous bending from 0 to 180°, without discernible invalidation after the battery recovered from drastic deformations like bending and twisting (**Figure 3b** and **Movie S1**). The galvanostatic discharge/charge curves in **Figure 3c,d** demonstrate that its electrochemical performance can be well maintained even if the battery was tolerating different deformations. Additionally, an 8 cm as-fabricated fiber-shaped energy device can assure a red LED of normal operation for over 10 h and still lighting even though it has been taken from pure CO<sub>2</sub> atmosphere into ambient environment (**Figure 3e**). The above phenomena verify the high energy density of this fiber-shaped Li-CO<sub>2</sub> battery and simultaneously describe the possibility of this device to become a real Li-air battery. Moreover, the unique 1D shape endows the battery with capability of being woven into textiles to prepare flexible self-powered fabric (**Figure 3f-i**), making it great potential on advanced energy accessories for wearable electronics. It is also noteworthy that the quasi-solid-state fiber-shaped battery exhibits good fire resistance owing to the utilization of fire-proof GPE (**Figure 3j,k**). In comparison, the control sample using traditional TEGDME-based liquid electrolyte is extremely easy to catch fire, as displayed in **Figure 3l,m**.

To better direct the catalyst design for Li-CO<sub>2</sub> battery in the future, a series of *in-situ/ex-situ* characterizations and DFT study were performed to understand the catalytic mechanism of CC@Mo<sub>2</sub>C NPs during cycling. As a dominant part of Li-CO<sub>2</sub> battery, the cathodes were analyzed in different discharge/charge stages. From the SEM images of **Figure 4a** and **4b**, a rough film with abundant worm-like nanosticks was reversibly formed and decomposed on

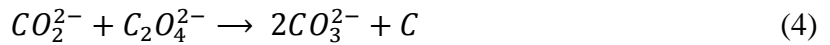
CC@Mo<sub>2</sub>C NPs electrode during cycling. Furthermore, Figure S17a,b show the XRD patterns of the discharged CNT cloth and CC@Mo<sub>2</sub>C NPs at the first cycle, respectively, which implies that that film observed in SEM was a certain kind of amorphous product instead of crystalline Li<sub>2</sub>CO<sub>3</sub> (the discharge product of pure CNTs). It is considered that this amorphous discharge product should have higher ionic conductivity than crystalline Li<sub>2</sub>CO<sub>3</sub> and some special radicals inside played a crucial role in reducing the charge potential. Therefore, to discern the underlying chemical state change happened on cathode during cycling, *in-situ* Raman spectroscopy was employed. As can be observed from Figure 4c, apart from those obvious signals belonging to CNTs, a small stretching peak of Mo-O bond gradually emerged and disappeared at around 920 cm<sup>-1</sup> as the discharge/charge steps proceeded. It implies that the amorphous film-like product stated above was combined with Mo<sub>2</sub>C nanoparticles in the form of Mo-O bond after discharging, while this Mo-O bond would break at the charge step allowing the evolution of CO<sub>2</sub> when discharged product decomposed. Moreover, we can also distinguish a quite broad and weak band at 1108~1271 cm<sup>-1</sup>, suggesting that the amorphous discharge product of CC@Mo<sub>2</sub>C NPs might be a certain intermediate toward lithium carbonate (1090 cm<sup>-1</sup>),<sup>[23]</sup> to some extent. Furthermore, *ex-situ* high-resolution X-ray photoelectron spectroscopy (XPS) analysis in Figure 4d-f depicts the dynamic regulation of Mo atoms between high-valence and low-valence state during cycling. It indicates that the outer electrons in Mo 3d orbit can reversibly transfer into strong electron acceptors (*c.a.* O atoms in CO<sub>2</sub> reduction products), which is in good accordance with the establishment and fracture of Mo-O bond presented in *in-situ* Raman spectroscopy. In addition, no peaks regarding to O=C-O can be observed in the XPS spectrum of C 1s orbit, further giving a proof that carbonate was not formed in this quasi-solid-state Li-CO<sub>2</sub> system (Figure S18).<sup>[23,34]</sup>

Based on the aforementioned results, it seems that a different reaction mechanism occurred in this quasi-solid-state Li-CO<sub>2</sub> battery using CC@Mo<sub>2</sub>C NPs as cathode. Providing that there

is also a preliminary reduction reaction which is analogous to classical Li-O<sub>2</sub> battery ( $O_2 + e^- \leftrightarrow O_2^-$ ),<sup>[24,34]</sup> a possible mechanism for this Li-CO<sub>2</sub> battery has been proposed:



In the initial step, CO<sub>2</sub> is firstly reduced to unstable C<sub>2</sub>O<sub>4</sub><sup>2-</sup> intermediate, as illustrated in Equation (1). Then, these C<sub>2</sub>O<sub>4</sub><sup>2-</sup> radicals can be connected with Mo<sub>2</sub>C by Mo-O chemical bond and through this metal-oxygen coupling, the outer electrons originated from Mo<sup>2+</sup> and Mo<sup>3+</sup> in Mo<sub>2</sub>C can be transferred into electronegative O atoms in C<sub>2</sub>O<sub>4</sub><sup>2-</sup>, leading to the increment of valence of Mo atoms.<sup>[34,40]</sup> It is believed that the above delocalized electrons contributed to stabilizing C<sub>2</sub>O<sub>4</sub><sup>2-</sup> and enabling the formation of Li<sub>2</sub>C<sub>2</sub>O<sub>4</sub> (Equation 2). During the charge process, Mo-O coupling dissociated and delocalized electrons returned to Mo atoms, which recovered the instability of C<sub>2</sub>O<sub>4</sub><sup>2-</sup>, as proved by *in-situ* Raman spectroscopy and *ex-situ* XPS. The unstable Li<sub>2</sub>C<sub>2</sub>O<sub>4</sub> is thermodynamically easier than Li<sub>2</sub>CO<sub>3</sub> to be decomposed ( $Li_2C_2O_4 \rightarrow 2Li^+ + 2CO_2 + 2e^-$ ,  $E^\circ = 3.01 \text{ V vs. Li/Li}^+$ )<sup>[41,42]</sup>, ( $2Li_2CO_3 \rightarrow 4Li^+ + O_2 + 2CO_2 + 4e^-$ ,  $E^\circ = 3.82 \text{ V vs. Li/Li}^+$ )<sup>[23]</sup>, and as a result, the charge potential was reduced to approximately 3.4 V,<sup>[24]</sup> as displayed in Figure 2c.



However, in the case of only CNTs as the catalyst, C<sub>2</sub>O<sub>4</sub><sup>2-</sup> would spontaneously split into CO<sub>3</sub><sup>2-</sup> and C *via* the disproportionation reactions of Equation (3) and Equation (4), without the coordination of electrons donator (Mo<sup>2+</sup> and Mo<sup>3+</sup> in this work). After Li<sup>+</sup> was extracted from electrolyte and combined with CO<sub>3</sub><sup>2-</sup>, solid Li<sub>2</sub>CO<sub>3</sub> was deposited on the surface of CNTs, shown in Equation (5). Owing to its insulating property and relatively high stability, Li<sub>2</sub>CO<sub>3</sub> is difficult to be decomposed below 4.0 V in practical experiments.<sup>[13,43]</sup>

A special precipitation method was employed to elucidate the existence of  $C_2O_4^{2-}$ , given that XRD measurement can not obtain its characteristic signals due to the amorphous property. It can be seen from Figure S19 that there were still some white precipitations in the solution containing discharge products of  $Mo_2C$ , while the one with that of CNT became clear, after the addition of  $CaCl_2$  and  $H_3PO_4$ .  $H_2C_2O_4$  seems to be the only stable acid consisting of only C, H and O elements of which the acidity is stronger than that of  $H_3PO_4$  at the same time. Therefore, it is reasonable to believe the discharge product of  $Mo_2C$  contained  $C_2O_4^{2-}$ , thus reinforcing the possibility of the above mechanism.

First-principles computations on basis of DFT were further implemented to confirm the possibility of generating  $Li_2C_2O_4$  intermediate stabilized by  $Mo_2C$ . According to the computational results of adsorption energy,  $Mo_2C$  exhibits more superior capture capability to Li and  $CO_2$  (-7.05 eV for Li/ $Mo_2C$  (001) and -6.84 eV for  $CO_2/Mo_2C$  (001)) than that of pure CNT (Figure S20 and S21).<sup>[44,45]</sup> Additionally, the electronic density of states (e-DOS) around the Fermi-level ( $E_f$ ) shows that the original metallic-like surface of  $Mo_2C$  still remains after Li and  $CO_2$  were adsorbed (Figure S22). These aforementioned results demonstrate that  $Mo_2C$  nanoparticles in CC@ $Mo_2C$  NPs can play as the active centers with high conductivity to effectively grasp the reactants of Li and  $CO_2$  as well as boosting the reaction progress. More importantly, it can be obtained from Figure 4g,h that  $Mo_2C$  makes a critical influence on stabilizing the intermediate discharge product  $Li_2C_2O_4$  and prevent its subsequent disproportionation reaction into  $CO_3^{2-}$ , although  $C_2O_4^{2-}$  is intrinsically unstable in terms of thermodynamics *per se* (-9.17 eV for  $Li_2C_2O_4/Mo_2C$  (001), -7.05 eV for  $Li_2CO_3/Mo_2C$  (001)). The stabilization can also be verified by charge density difference in Figure 4k. The outer electrons of  $Mo_2C$  (electrons donator) have transferred into O atoms (electrons acceptor) in  $Li_2C_2O_4$  in the optimized structure after adsorption, thus facilitating the fast stabilization of intermediate discharge product by delocalized electrons, while the electrons transfer between  $Li_2CO_3$  and  $Mo_2C$  is not so much obvious (Figure S23), well consistent with the results of

experiments. In comparison, there is an immense obstacle for individual CNT to serve the same function. Because of lacking electrons transfer (Figure 4i),  $\text{Li}_2\text{C}_2\text{O}_4$  could not exist as a long-term product on CNT surface ( $E_{\text{ads}}(\text{Li}_2\text{C}_2\text{O}_4/\text{CNT}_{(002)}) = 1.05 \text{ eV}$ , Figure 4i). Nevertheless, owing to the weak contribution derived from outer electrons of carbon atoms (Figure S24), thermodynamically stable  $\text{Li}_2\text{CO}_3$  can steadily deposit on the surface of CNTs without further phase transformation ( $E_{\text{ads}}(\text{Li}_2\text{CO}_3/\text{CNT}_{(002)}) = -1.67 \text{ eV}$ , Figure 4j). Therefore, it is considered that  $\text{Li}_2\text{C}_2\text{O}_4$  and  $\text{Li}_2\text{CO}_3$  are the different discharge products of  $\text{CC@Mo}_2\text{C}$  NPs and CNT cloth, respectively.

In summary, we have developed an **quasi-solid-state** flexible fiber-shaped Li- $\text{CO}_2$  battery using specially designed free-standing CNT/ $\text{Mo}_2\text{C}$  hybrid film as the cathode. Benefiting from the unique porous structure and high catalytic activity, the newly-developed **quasi-solid-state** Li- $\text{CO}_2$  batteries exhibited a significantly reduced charge potential below 3.4 V, a large area specific capacity and **an enhanced** cycle performance. The energy efficiency of the battery has been raised to ~80% which is the highest among all previously reported Li- $\text{CO}_2$  batteries. The as-fabricated 1D **quasi-solid-state** battery also demonstrated superior flexibility and could maintain normal function even suffering various drastic deformations. It was found that  $\text{Mo}_2\text{C}$  nanoparticles in hybrid film could efficiently stabilize the amorphous intermediate discharge product  $\text{Li}_2\text{C}_2\text{O}_4$  through coordinative electrons transfer, **thus leading to a declined charge voltage plateau. We hope that this work can offer some inspirations on catalyst design for Li- $\text{CO}_2$  batteries in the future. Apart from developing rare-earth metal based catalysts like Ru,<sup>[21,23,46]</sup> Ir<sup>[47,48]</sup> which improve the reversibility of  $\text{Li}_2\text{CO}_3$  decomposition, transition metal carbides with metal atoms in intermediate valence seem to be a more cost-effective and promising candidate, since it may stabilize the  $\text{CO}_2\text{RR}$  at the 2-electrons transfer stage and prevent the subsequent disproportionation processes toward 4-electrons transfer, which remarkably shortens the overpotential of current Li- $\text{CO}_2$  battery systems. Additionally, this work also verified the possibilities of using efficient, **binder-free** and free-standing hybrid**

catalysts to construct 1D **quasi-solid-state** flexible fiber-shaped Li-CO<sub>2</sub> batteries with enhanced energy efficiency, eliminating a major obstacle and accelerating the technology progress of Li-CO<sub>2</sub> battery toward practical application.

### Supporting Information

Supporting Information is available from the Wiley Online Library or from the author.

### Acknowledgements

The authors acknowledge the financial support by the National Natural Science Foundation of China (No. 21875226, 21501160 and 51741305), the Science Foundation for Distinguished Young Scholars of Sichuan Province (2016JQ0025 and 2017JQ0036), the Chengdu Rongpiao Talent plan, the “QianYingBaiTuan” Plan of China Mianyang Science City, the Science Foundation of Institute of Chemical Materials (No.011100301) and the “1000plan” from the Chinese Government. J. Lu gratefully acknowledges support from the U. S. Department of Energy (DOE), Office of Energy Efficiency and Renewable Energy, Vehicle Technologies Office. Argonne National Laboratory is operated for DOE Office of Science by UChicago Argonne, LLC, under contract number DE-AC02-06CH11357. The authors specially appreciate to the spiritual support of Miss. Huihui Lu from Prof. Naiqin Zhao’s group at Tianjin University, as well as the technical advice of Dr. Tianshuai Wang from Beihang University.

Received: ((will be filled in by the editorial staff))

Revised: ((will be filled in by the editorial staff))

Published online: ((will be filled in by the editorial staff))

### References

- [1] B. Kang and G. Ceder, *Nature* **2009**, *458*, 190.
- [2] F. Cheng, J. Liang, Z. Tao and J. Chen, *Adv. Mater.*, **2011**, *23*, 1695.
- [3] J. Zhou, J. Qin, X. Zhang, C. Shi, E. Liu, J. Li, N. Zhao and C. He, *ACS Nano* **2015**, *9*, 3837.
- [4] H. Sun, Y. Zhang, J. Zhang, X. Sun and H. Peng, *Nat. Rev. Mater.* **2017**, *2*, 17023.
- [5] Y. Li, C. Zhong, J. Liu, X. Zeng, S. Qu, X. Han, Y. Deng, W. Hu and J. Lu, *Adv. Mater.* **2018**, *30*, 1703657.
- [6] Y. Zhang, L. Wang, Z. Guo, Y. Xu, Y. Wang and H. Peng, *Angew. Chem., Int. Ed.* **2016**, *55*, 4487.

- [7] X. Chen, C. Zhong, B. Liu, Z. Liu, X. Bi, N. Zhao, X. Han, Y. Deng, J. Lu and W. Hu, *Small*, **2018**, 1702987.
- [8] X. Chen, B. Liu, C. Zhong, Z. Liu, J. Liu, L. Ma, Y. Deng, X. Han, T. Wu, W. Hu and J. Lu, *Adv. Energy Mater.* **2017**, 7, 1700779.
- [9] S. Xu, S. K. Das and L. A. Archer, *RSC Adv.* **2013**, 3, 6656.
- [10] K. Takechi, T. Shiga and T. Asaoka, *Chem. Commun.* **2011**, 47, 3463.
- [11] X. Zhang, Q. Zhang, Z. Zhang, Y. Chen, Z. Xie, J. Wei and Z. Zhou, *Chem. Commun.* **2015**, 51, 14636.
- [12] A. Vasileff, Y. Zheng and S. Z. Qiao, *Adv. Energy Mater.* **2017**, 7, 1700759.
- [13] Z. Xie, X. Zhang, Z. Zhang and Z. Zhou, *Adv. Mater.* **2017**, 29, 1605891.
- [14] L. Qie, Y. Lin, J. W. Connell, J. Xu and L. Dai, *Angew. Chem., Int. Ed.* **2017**, 56, 6970.
- [15] Y. Liu, R. Wang, Y. Lyu, H. Li and L. Chen, *Energy Environ. Sci.* **2014**, 7, 677.
- [16] X. Hu, Z. Li and J. Chen, *Angew. Chem., Int. Ed.* **2017**, 56, 5785.
- [17] Z. Zhang, Q. Zhang, Y. Chen, J. Bao, X. Zhou, Z. Xie, J. Wei and Z. Zhou, *Angew. Chem., Int. Ed.* **2015**, 54, 6550.
- [18] Z. Zhang, X. G. Wang, X. Zhang, Z. Xie, Y. N. Chen, L. Ma, Z. Peng and Z. Zhou, *Adv. Sci.* **2018**, 5, 1700567.
- [19] H. Lim, H. Lim, K. Park, D. Seo, H. Gwon, J. Hong, W. Goddard, H. Kim and K. Kang, *J. Am. Chem. Soc.* **2013**, 135, 9733.
- [20] Z. Zhang, Z. Zhang, P. Liu, Y. Xie, K. Cao and Z. Zhou, *J. Mater. Chem. A* **2018**, 6, 3218.
- [21] S. Yang, Y. Qiao, P. He, Y. Liu, Z. Cheng, J. Zhu and H. Zhou, *Energy Environ. Sci.* **2017**, 10, 972.
- [22] X. Zhang, C. Wang, H. Li, X. Wang, Y. Chen, Z. Xie and Z. Zhou, *J. Mater. Chem. A* **2018**, 6, 2792.
- [23] Y. Qiao, J. Yi, S. Wu, Y. Liu, S. Yang, P. He and H. Zhou, *Joule*, **2017**, 1, 359.
- [24] Y. Hou, J. Wang, L. Liu, Y. Liu, S. Chou, D. Shi, H. Liu, Y. Wu, W. Zhang and J. Chen,

- Adv. Funct. Mater.* **2017**, *27*, 1700564.
- [25] Q. Zhu, S. Xu, Z. Cai, M. M. Harris, K. Wang and J. Chen, *Energy Storage Mater.* **2017**, *7*, 209.
- [26] X. Fang, W. Weng, J. Ren and H. Peng, *Adv. Mater.* **2016**, *28*, 491.
- [27] Y. Zhang, Y. Zhao, J. Ren, W. Weng and H. Peng, *Adv. Mater.* **2016**, *28*, 4524.
- [28] Y. Xu, Y. Zhao, J. Ren, Y. Zhang and H. Peng, *Angew. Chem., Int. Ed.* **2016**, *55*, 7979.
- [29] L. Wang, J. Pan, Y. Zhang, X. Cheng, L. Liu and H. Peng, *Adv. Mater.* **2018**, *30*, 1704378.
- [30] Y. B. Yin, X. Y. Yang, Z. W. Chang, Y. H. Zhu, T. Liu, J. M. Yan and Q. Jiang, *Adv. Mater.* **2018**, *30*, 1703791.
- [31] C. Li, Z. Guo, B. Yang, Y. Liu, Y. Wang and Y. Xia, *Angew. Chem., Int. Ed.* **2017**, *129*, 9254.
- [32] X. Hu, Z. Li, Y. Zhao, J. Sun, Q. Zhao, J. Wang, Z. Tao and J. Chen, *Sci. Adv.* **2017**, *3*, e1602396.
- [33] J. Guo, J. Wang, C. Xuan, Z. Wu, W. Lei, J. Zhu, W. Xiao and D. Wang, *J. Electroanal. Chem.* **2017**, *801*, 7.
- [34] W.-J. Kwak, K. C. Lau, C.-D. Shin, K. Amine, L. A. Curtiss and Y.-K. Sun, *ACS Nano*, **2015**, *9*, 4129.
- [35] D.-H. Youn, S.-H. Han, J. Y. Kim, J. Y. Kim, H.-M. Park, S. H. Choi and J. S. Lee, *ACS Nano*, **2014**, *8*, 5164.
- [36] Y. Chen, Y. Zhang, W. Jiang, X. Zhang, Z. Dai, L. Wan and J. Hu, *ACS Nano*, **2016**, *10*, 8851.
- [37] F. X. Ma, H. B. Wu, B. Y. Xia, C. Y. Xu and X. W. Lou, *Angew. Chem., Int. Ed.* **2015**, *54*, 15395.
- [38] Z. Y. Yu, Y. Duan, M. R. Gao, C. C. Lang, Y. R. Zheng and S. H. Yu, *Chem. Sci.* **2017**, *8*, 968.
- [39] J. Ren, Y. Zhang, W. Bai, X. Chen, Z. Zhang, X. Fang, W. Weng, Y. Wang and H. Peng, *Angew. Chem., Int. Ed.* **2014**, *53*, 7864.

- [40] Y. Hou, Y. Liu, Z. Zhou, L. Liu, H. Guo, H. Liu, J. Wang and J. Chen, *Electrochim. Acta* **2018**, *259*, 313.
- [41] R. Angamuthu, P. Byers, M. Lutz, A. L. Spek and E. Bouwman, *Science*, **2010**, *327*, 313.
- [42] K. Németh and G. Srajer, *RSC Adv.* **2014**, *4*, 1879.
- [43] B. Huang and G. Frapper, *J. Am. Chem. Soc.* **2018**, *140*, 413.
- [44] R. Kannan, U. Bipinlal, S. Kurungot and V. K. Pillai, *Phys. Chem. Chem. Phys.* **2011**, *13*, 10312.
- [45] Y. Jing and Z. Zhou, *ACS Catal.* **2015**, *5*, 4309.
- [46] S. Xu, Z. Ren, X. Liu, X. Liang, K. Wang and J. Chen, *Energy Storage Mater.* **2018**, *18*, 291.
- [47] C. Wang, Q. Zhang, X. Zhang, X. Wang, Z. Xie and Z. Zhou, *Small* **2018**, *14*, 1800641.
- [48] Y. Mao, C. Tang, Z. Tang, J. Xie, Z. Chen, J. Tu, G. Cao and X. Zhao, *Energy Storage Materials* **2018**, <https://doi.org/10.1016/j.ensm.2018.08.011>.

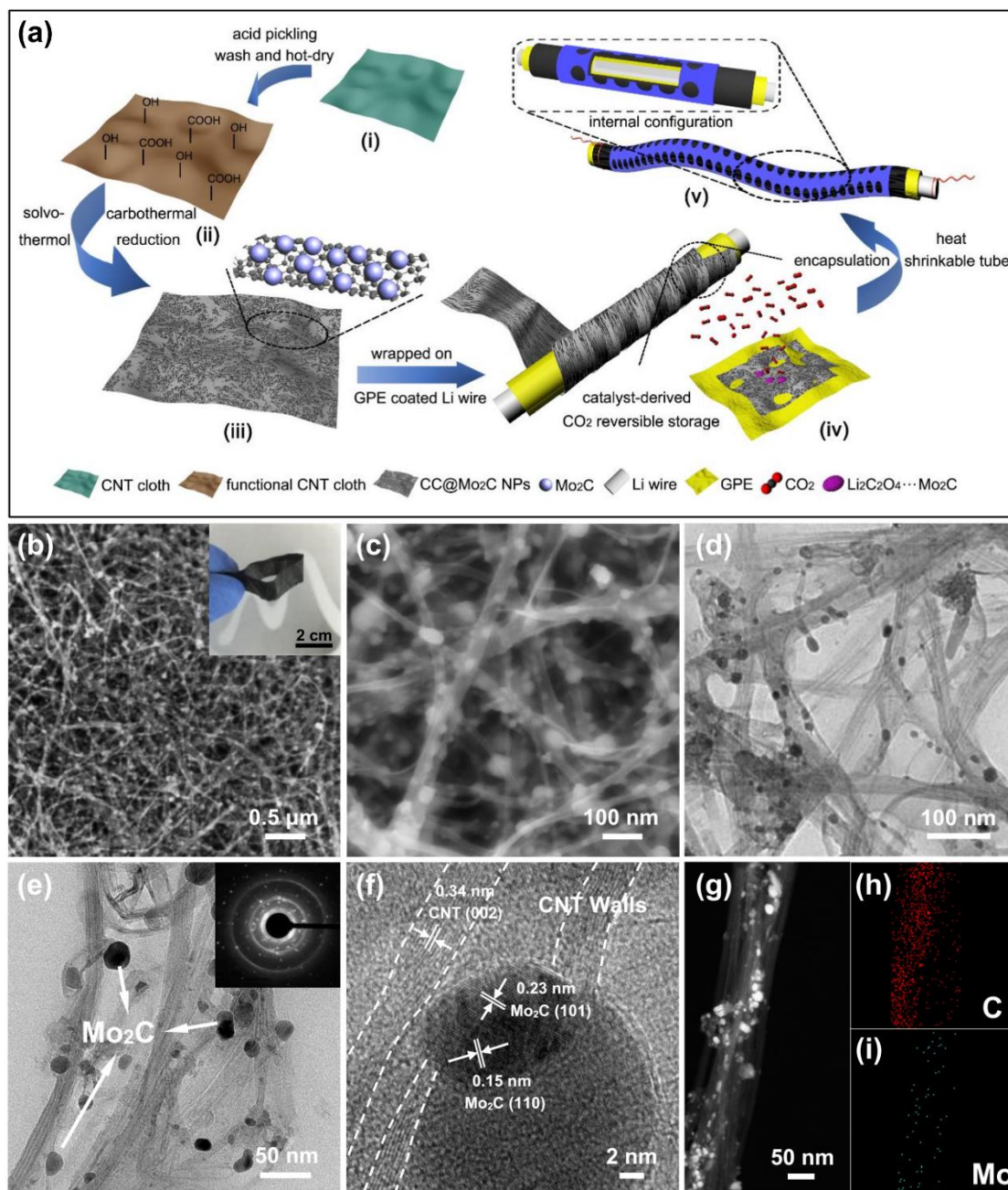


**Figure 1.** (a) Schematics illustrating the preparation procedure of the quasi-solid-state flexible fiber-shaped Li-CO<sub>2</sub> battery with CC@Mo<sub>2</sub>C NPs free-standing film as working electrode: (i) Pristine highly conductive CNT cloth. (ii) Functional CNT cloth with abundant hydrophilic radicals. (iii) CNT cloth anchored with homogeneously distributed Mo<sub>2</sub>C nanoparticles. (iv) The gel polymer electrolyte coated lithium wire which is wrapped by CC@Mo<sub>2</sub>C NPs. (v) As-fabricated flexible fiber-shaped Li-CO<sub>2</sub> battery. (b,c) SEM images of CC@Mo<sub>2</sub>C NPs with an optical photo inset in (b). (d,e) TEM and (f) HRTEM images of CC@Mo<sub>2</sub>C NPs, with a corresponding SAED pattern inside in (e). (g) STEM and element mappings of (h) C and (i) Mo of a typical CNT anchored with ultrafine Mo<sub>2</sub>C nanoparticles extracted from the hybrid film.

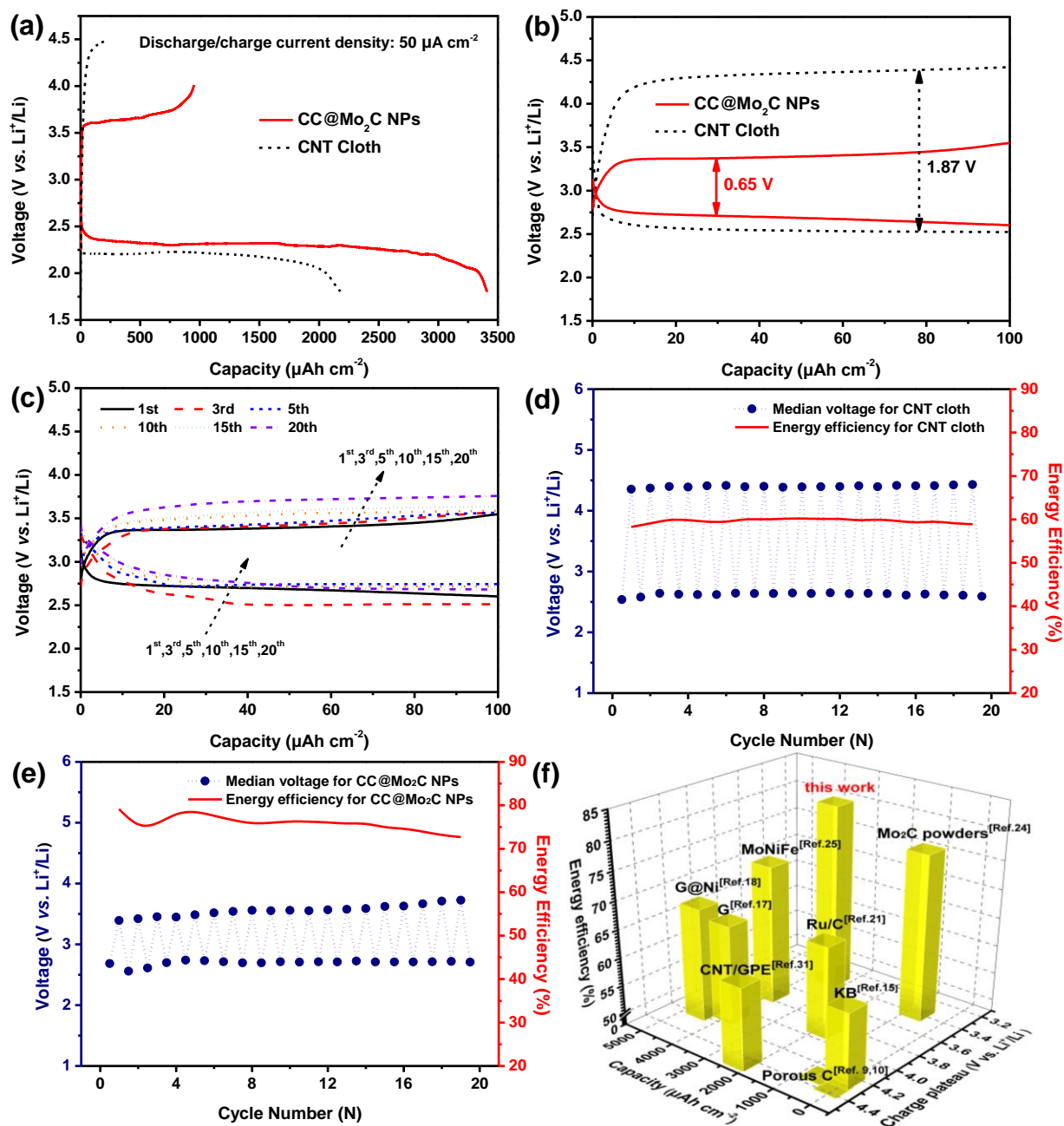


**Figure 2.** (a) Galvanostatic discharge/charge profiles of CC@Mo<sub>2</sub>C NPs and CNT cloth under CO<sub>2</sub> at a current density of 50 μA cm<sup>-2</sup>. (b) Comparison of the galvanostatic discharge/charge profiles of CC@Mo<sub>2</sub>C NPs and CNT cloth electrodes in CO<sub>2</sub> within the initial capacity of 100 μAh cm<sup>-2</sup>. (c) Cycling behavior of CC@Mo<sub>2</sub>C NPs electrode for the selected cycles under CO<sub>2</sub> at a current of 20 μA cm<sup>-2</sup> and curtailing capacity of 100 μAh cm<sup>-2</sup>. Median voltages of discharge/charge plateaus for (d) CNT cloth and (e) CC@Mo<sub>2</sub>C NPs electrodes. The red line inset refers to energy efficiency, directly revealing the proportion of energy loss during the repeated storage and release of electricity. (f) The comparison of different cathode materials for Li-CO<sub>2</sub> batteries in the aspects of area specific capacity, charge plateau and energy efficiency.

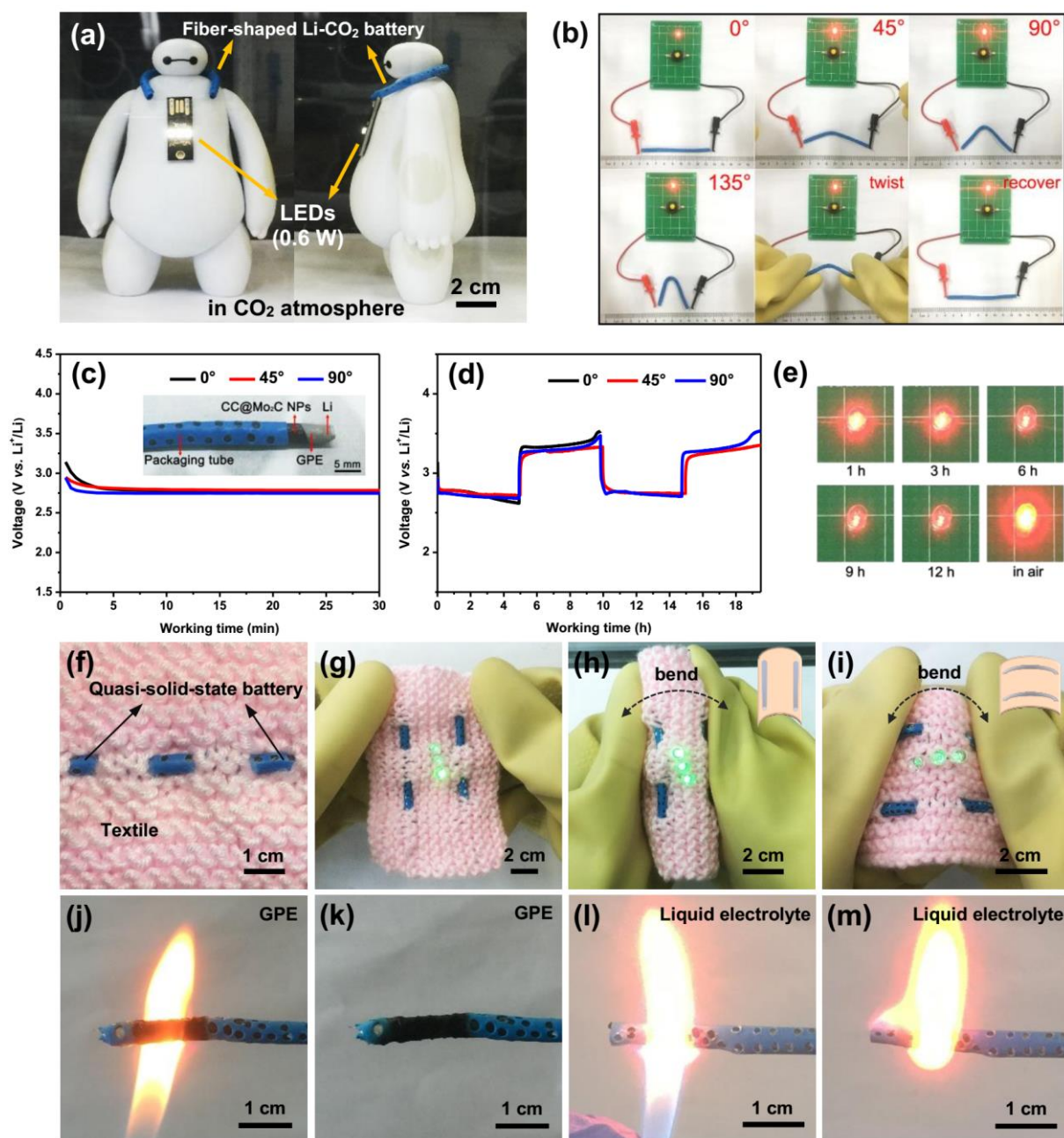


**Figure 3.** (a) Digital photograph depicting the wearability of as-fabricated quasi-solid-state flexible fiber-shaped Li-CO<sub>2</sub> battery which lit up three high-power LEDs (0.6 W) on a toy. (b) A red LED lit up by the battery under different bending and twisting deformations. (c,d) Galvanostatic discharge/charge curves of the quasi-solid-state flexible fiber-shaped battery at the bending angles of 0°, 45° and 90° under 20 μA, with a photograph depicting the configuration of the battery inset. (e) A red LED powered by an 8 cm fiber-shaped Li-CO<sub>2</sub> battery for 12 h and then exposed to ambient air. (f,g) A textile integrated with double fiber-shaped Li-CO<sub>2</sub> battery as power accessory. (h,i) Three green LEDs lit up by the self-powered textile which was bent at different directions (along and vertical to the battery). Fire-proof properties of (j,k) the quasi-solid-state fiber-shaped battery using GPE and (i,m) the traditional fiber-shaped battery using liquid electrolyte.

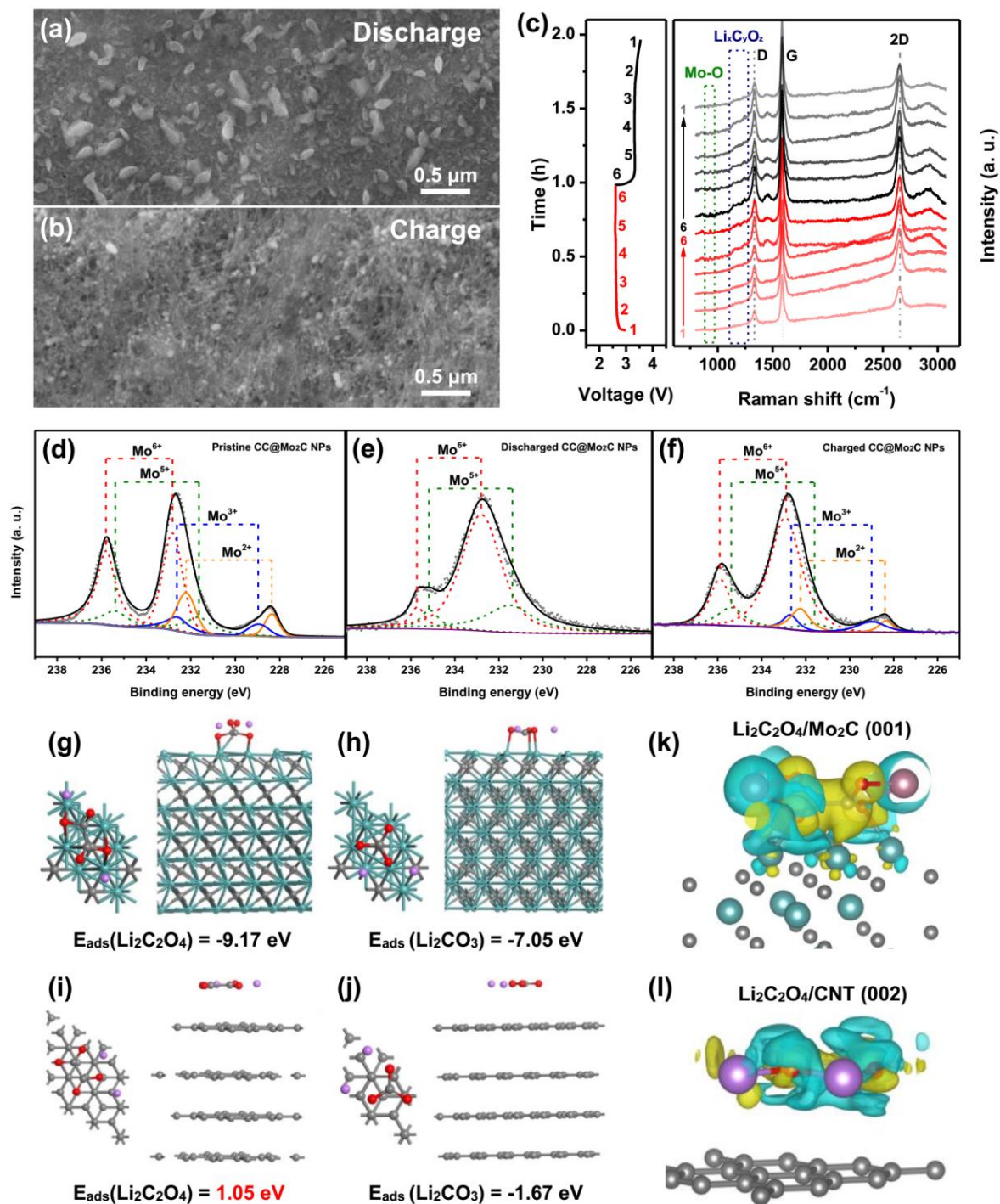


**Figure 4.** Typical SEM images of CC@Mo<sub>2</sub>C NPs after (a) the first discharge process and (b) the charge process with a current density of 20 μA cm<sup>-2</sup>, curtailing capacity of 100 μAh cm<sup>-2</sup>. (c) The *in-situ* Raman spectra of CC@Mo<sub>2</sub>C NPs electrode at 12 selected states during cycling at 20 μA cm<sup>-2</sup> with corresponding discharge/charge profiles on the left. The high-resolution XPS spectra of Mo 3d for CC@Mo<sub>2</sub>C NPs at different states: (d) pristine, (e) discharged and (f) recharged. Top (left) and side (right) view of the optimized energetically most favorable structures of (g) Li<sub>2</sub>C<sub>2</sub>O<sub>4</sub>, (h) Li<sub>2</sub>CO<sub>3</sub> adsorbed on Mo<sub>2</sub>C (001) surface and (i) Li<sub>2</sub>C<sub>2</sub>O<sub>4</sub>, (j) Li<sub>2</sub>CO<sub>3</sub> adsorbed on CNT (002) surface. The cyan, purple, grey and red balls represent Mo, Li,

C and O, respectively. Charge density difference of  $\text{Li}_2\text{C}_2\text{O}_4$  adsorbed on (k)  $\text{Mo}_2\text{C}$  (001) surface and (l) CNT (002) surface, respectively. The yellow and light blue regions represent the charge accumulation and charge loss, respectively. The isosurface value is set to be  $0.007 \text{ e}/\text{\AA}^3$ .

**Keyword**

quasi-solid-state, fiber-shaped, flexible, Li- $\text{CO}_2$  batteries, low overpotential

**A Quasi-Solid-State Flexible Fiber-shaped Li- $\text{CO}_2$  Battery with Low Overpotential and High Energy Efficiency**

ToC figure



## Supporting Information

### **A **Quasi-Solid-State** Flexible Fiber-shaped Li-CO<sub>2</sub> Battery with Low Overpotential and High Energy Efficiency**

*Jingwen Zhou, Xuelian Li, Chao Yang, Yinchuan Li, Kunkun Guo, Jianli Cheng\*, Dingwang Yuan, Chenhui Song, Jun Lu\* and Bin Wang\**

## Experimental Section

*Synthesis of CC@Mo<sub>2</sub>C NPs free-standing film:* CC@Mo<sub>2</sub>C NPs free-standing film was prepared through a modified solvothermal method, followed by an *in-situ* CVD conversion process. Highly conductive CNT cloth purchased from Chengdu Institute of Organic Chemistry was successively washed by acetone, alcohol and distilled water before used. To introduce abundant hydrophilic radicals, the clean CNT cloth was immersed in 30%<sub>vol</sub> nitric acid solution for 12 h, which was then cleaned with distilled water for several times. In a typical synthesis, 90 mg of (NH<sub>4</sub>)<sub>6</sub>Mo<sub>7</sub>O<sub>24</sub>·4H<sub>2</sub>O was first dissolved in a mixture of 10 ml deionized water and 20 ml ethylene glycol by magnetic stirring. Several pieces of functional CNT cloth were added into the as-obtained homogeneous solution, with ultrasonic treatment for 30 min. Subsequently, those functional CNT cloth pieces were transferred to a 50 ml Teflon-lined stainless steel autoclave and kept in an oven at 200 °C for 10 h. After cooling down naturally, CNT cloth coated by evenly distributed low-crystalline MoO<sub>2</sub> layers (CC@LC-MoO<sub>2</sub>) was collected, washed with deionized water and freeze-dried. During the *in-situ* conversion procedure, CC@LC-MoO<sub>2</sub> was placed in a quartz boat located in the middle of the furnace tube and then calcinated at 850 °C for 2 h in H<sub>2</sub> (5%)/Ar (95%) atmosphere at a gas flow of 200 sccm, with the heating rate of 10 °C min<sup>-1</sup>. The free-standing and flexible CNT cloth with highly dispersed Mo<sub>2</sub>C nanoparticles (CC@Mo<sub>2</sub>C NPs) was obtained after the furnace was cooled down to room temperature under the protection of Ar. The content of Mo<sub>2</sub>C component in the composite film can be easily controlled by adjusting the amount of ammonium molybdate employed for solvothermal growth.

*Preparation of gel polymer electrolyte (GPE):* Lithium bis(trifluoromethane sulfonimide) (LiTFSI), tetraglyme (TEGDME), poly(vinylidene fluoride-co-hexafluoropropylene) (PVDF-HFP, average Mn of ~130000), N-methyl-2-pyrrolidinone (NMP, 99.5 %), 2-hydroxy-2-methyl-1-phenyl-1-propanone (HMPP, 97 %) and trimethylolpropane ethoxylate triacrylate

(TMPET, average  $M_n$  of  $\sim 428$ ) were purchased from Sigma and used without further purification. All reagents were operated in an argon-filled glovebox. Firstly, 2.4 g LiTFSI was dissolved in 1.6 g TEGDME to generate a transparent solution A. Then, 4.0 g NMP was mixed with 1.0 g PVDF-HFP under continuous stirring until the mixture became a kind of homogeneous and viscous liquid (Solution B). 0.01 g HMPP was introduced into 3.0 g TMPET by stirring to constitute Solution C. It was noteworthy that Solution C should be prepared when assembling Li-CO<sub>2</sub> batteries and stored in a brown glass bottle. An ivory slurry (GPE precursor) was formed by the mixing of Solution A, B and C at a weight ratio of 4:5:3. The result GPE was solidified by the irradiation of UV-light for 15 s.

*Li-CO<sub>2</sub> cells and fiber-shaped devices assembly:* Free-standing CC@Mo<sub>2</sub>C NPs and pristine highly conductive CNT cloth were both tailored into 1×1 cm square electrode before the assembly of coin-type Li-CO<sub>2</sub> cells in an Ar-filled glovebox with O<sub>2</sub> and H<sub>2</sub>O contents less than 1 ppm. The average weight of square CC@Mo<sub>2</sub>C NPs and CNT cloth are 1.0 mg and 0.6 mg, respectively. Lithium metal foil acted as both counter and reference electrode. CC@Mo<sub>2</sub>C NPs (or CNT cloth) cathode was separated from lithium foil by GPE membrane aforementioned. A stainless steel mesh (SSM) was covered on CC@Mo<sub>2</sub>C NPs (or CNT cloth), playing a role of gas diffusion layer. In the following, the whole configuration of Li anode/GPE/CC@Mo<sub>2</sub>C NPs (or CNT cloth)/SSM was sealed into a Swagelok cell with a hole (approximately 0.785 cm<sup>2</sup>) on the center of cathode side. As for the fabrication of **quasi-solid-state** flexible fiber-shaped devices, one-dimensional (1D) lithium wire with an average diameter of 3.2 mm was used to substitute lithium foil existing in 2D planar devices, which not only worked as anode but also provided a substrate for the next construction of 1D fiber-shaped Li-CO<sub>2</sub> batteries. Lithium wire with a certain length was dipped in the mixed GPE precursor slurry and slowly rotated until the precursor gel was even covered on the whole surface of lithium wire. The precursor slurry formed solidified GPE layer intimately bonded with lithium metal after receiving the irradiation

of UV-light. To avoid possible risk of short circuit, the above procedure was repeated three times. After that, as-prepared CC@Mo<sub>2</sub>C NPs free-standing film was carefully wrapped on the GPE coated lithium wire. Finally, the fiber-shaped battery was encapsulated inside an adaptable shrinkable tube with sufficient holes for protection.

*Material Characterizations:* XRD measurements were conducted on a Bruker D2 diffractometer using Cu KR radiation at a wavelength of 1.5406 Å. SEM was performed on a JSM-6700F scanning electron microscope. FEI Tecnai G<sup>2</sup> F20 field emission transmission electron microscope was employed to carry out TEM, HRTEM, STEM and elemental mappings. TG analysis was implemented using a PerkinElmer (TA Instruments) up to 800 °C with a heating rate of 10 °C min<sup>-1</sup> in oxygen. Raman spectrum was recorded on the LabRAM HR Raman spectrometer with laser excitation at 514.5 nm from an Ar ion laser source. XPS analysis was based on an ESCALab220i-XL electron spectrometer from VG Scientific using 300 W Al KR radiation.

*Electrochemical Tests:* All electrochemical performances were executed in a dried chamber which was filled with pure CO<sub>2</sub> gas. Considering the sufficient diffusion of CO<sub>2</sub> into solidified GPE, the **quasi-solid-state** Li-CO<sub>2</sub> batteries had been placed in the CO<sub>2</sub>-filled chamber and allowed a rest period of 10 h for stabilization before tests. CV was conducted on a CHI660D electrochemical workstation at a scan rate of 0.2 mV s<sup>-1</sup> over the potential window of 1.8-4.2 V vs. Li<sup>+</sup>/Li. The galvanostatic discharge/charge measurements of these Li-CO<sub>2</sub> batteries were carried out on a LAND CT2001A electrochemical workstation under different test parameters at room temperature.

*DFT Calculations:* The thermodynamically abundant (001) and (101) surfaces of Mo<sub>2</sub>C which are dominant on the Wulff crystal have been established. For comparison, bare CNT (002)

surface was also considered in the simulations, simultaneously. All the simulations are performed on basis of Density Functional Theory (DFT) calculations with plane-wave technique which is implemented in the Vienna ab initio simulation package (VASP). Gradient corrected exchange-correlation functional of Perdew, Burke, and Ernzerhof (PBE) models were employed to proceed the spin-polarized calculations under the projector augmented wave (PAW) method, with a cut-off kinetic energy of 400 eV for plane wave basis. The convergence criterion of the total energy was set up to be within  $1 \times 10^{-5}$  eV, while all the atoms and geometries were optimized until the residual forces became less than  $1 \times 10^{-2}$  eV/Å. For hexagonal Mo<sub>2</sub>C and carbon nanotube crystals, these optimized energetically most favorable structures after the full geometry relaxation were implemented within a K-point  $5 \times 5 \times 5$  grid. In consideration of weak interaction between layers, DFT-D3 method with Beck-Jonson damping was adopted in the calculation. For all the surfaces-related calculations including the adsorption of atoms and molecules on Mo<sub>2</sub>C (001) (101) and CNT (002) surfaces, they were carried out within a K-point  $5 \times 5 \times 1$  grid. For each of the modeling surfaces, the surface thicknesses are controlled to approximately 12~15 Å to ensure the required energy convergence during the whole simulation process. The adsorption energy of Li/CO<sub>2</sub>/Li<sub>2</sub>C<sub>2</sub>O<sub>4</sub>/Li<sub>2</sub>CO<sub>3</sub> is defined as  $E_{ads} = E_T - E_A - E_S$ , where  $E_T$  is the total energy of the corresponding system with specified atoms or molecules adsorbed;  $E_A$  and  $E_S$  represent the energy of the specified atom or molecule and the pristine system, respectively.

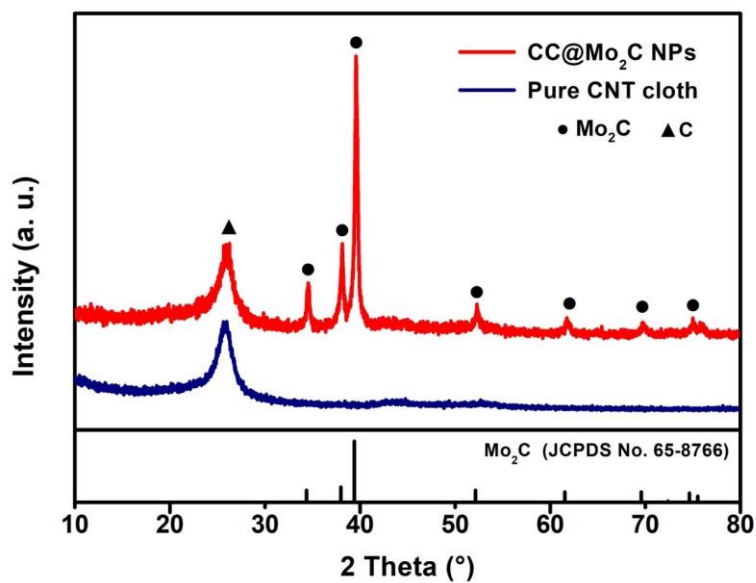


**Figure S1.** XRD patterns of the as-synthesized CC@Mo<sub>2</sub>C NPs free-standing film and the pristine CNT cloth.

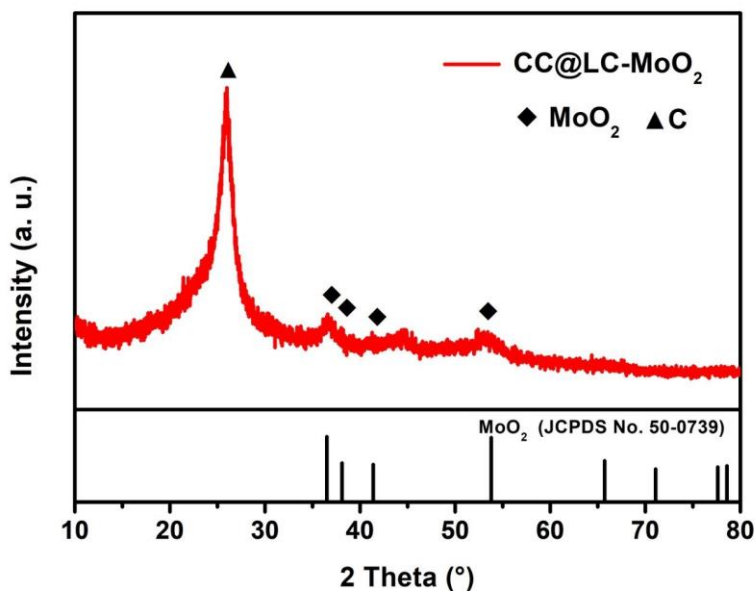


**Figure S2.** XRD pattern of the CNT cloth attached with low-crystalline MoO<sub>2</sub> layers (denoted as CC@LC-MoO<sub>2</sub>) after the solvothermal growth process.

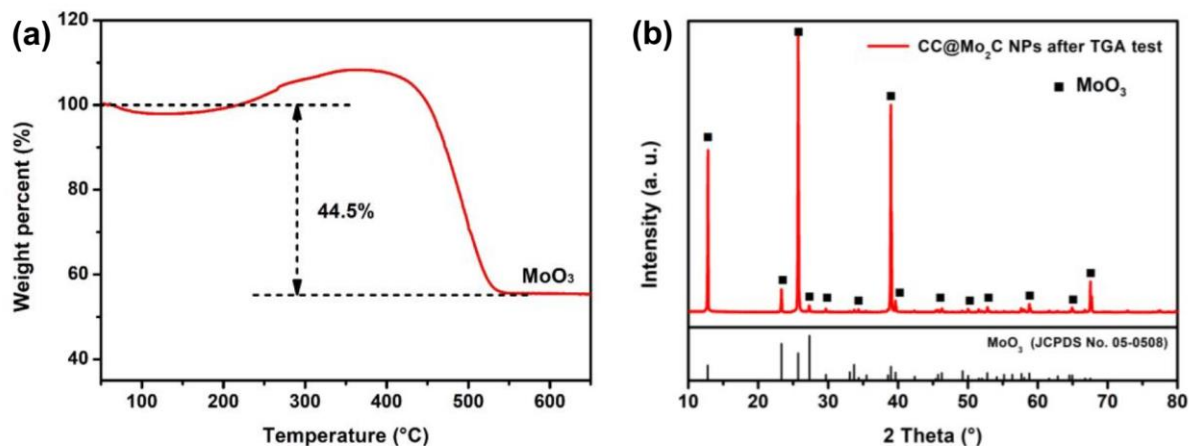


**Figure S3.** (a) TG curve of the as-synthesized CC@Mo<sub>2</sub>C NPs free-standing film, with the highest temperature set to be 650 °C at a heating rate of 10 °C min<sup>-1</sup> in ambient air. (b) The XRD pattern of the sample after TG measurement, exhibiting the typical diffraction peaks of MoO<sub>3</sub> with high purity.

After the as-synthesized CC@Mo<sub>2</sub>C NPs free-standing film was heated to 650 °C in ambient air, the sample was completely converted into pure MoO<sub>3</sub> powders, leading to a weight loss of 44.5% compared with the original composite film. The weight loss should be attributed to both the disappearance of CNTs and the oxidation of Mo<sub>2</sub>C to MoO<sub>3</sub>.

Assuming that the contents of Mo<sub>2</sub>C and CNTs are  $a$  and  $b$  in the CC@Mo<sub>2</sub>C NPs, the relationship between these two parameters can be illustrated as the following equations:

$$a + b = 1 \quad (1)$$

$$\frac{ma}{a+b} = 1 - 44.5\% \quad (2)$$

The constant parameter  $m$  should be obtained based on the weight increase when 1 Mol Mo<sub>2</sub>C (relative molecular mass: 203.88) is fully oxidized into 2 Mol MoO<sub>3</sub> (Relative molecular mass: 143.94). Therefore,  $m$  should be 1.412 in this case. Accordingly,  $a$  and  $b$  can be worked out by solving the above two equations. Hence, the content of Mo<sub>2</sub>C in the composite film is calculated to be approximately 39.3% on a weight basis.

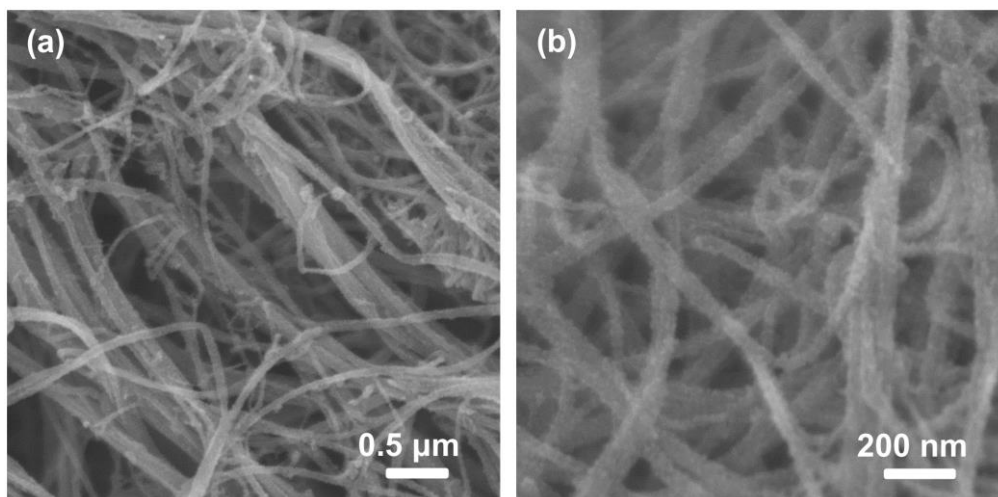


**Figure S4.** Typical SEM images of the CC@LC-MoO<sub>2</sub> in (a) low and (b) high magnification, respectively, indicating that plenty of ultrafine nanoparticles were formed into a homogeneous layer anchored on the surface of CNTs.

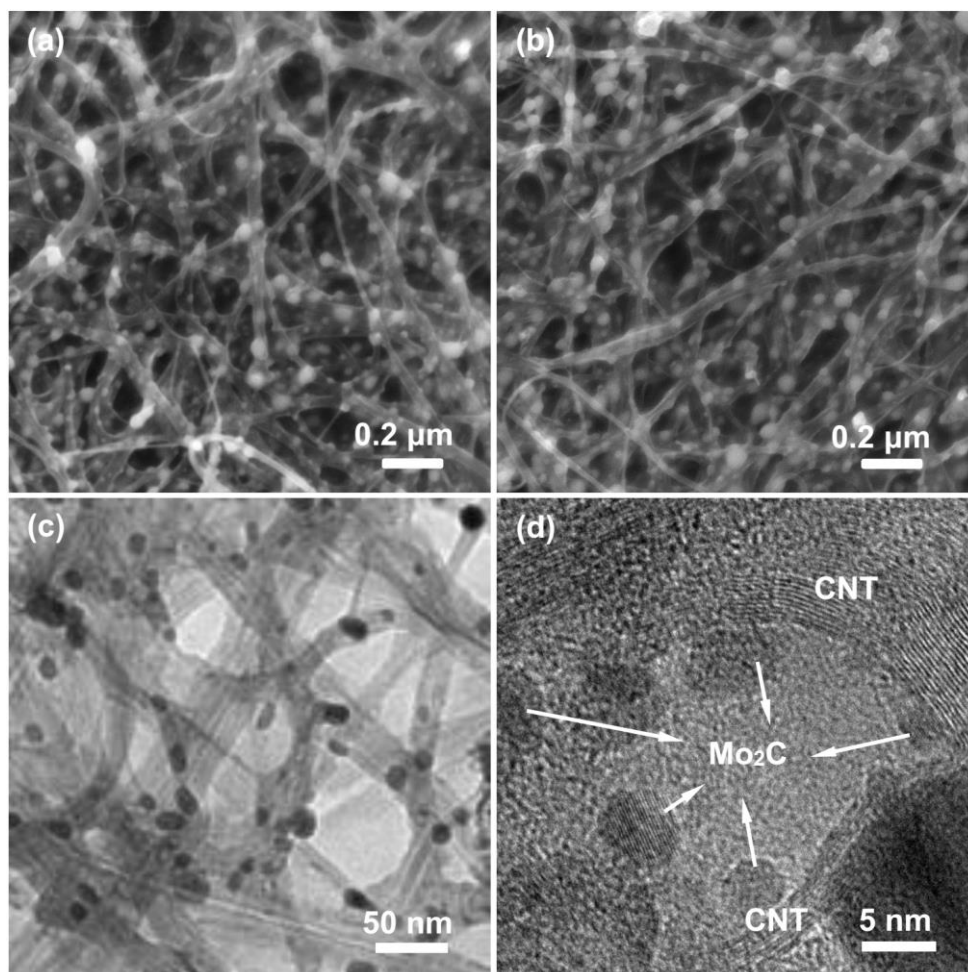


**Figure S5.** (a,b) Typical SEM and (c,d) TEM images of the CC@Mo<sub>2</sub>C NPs.

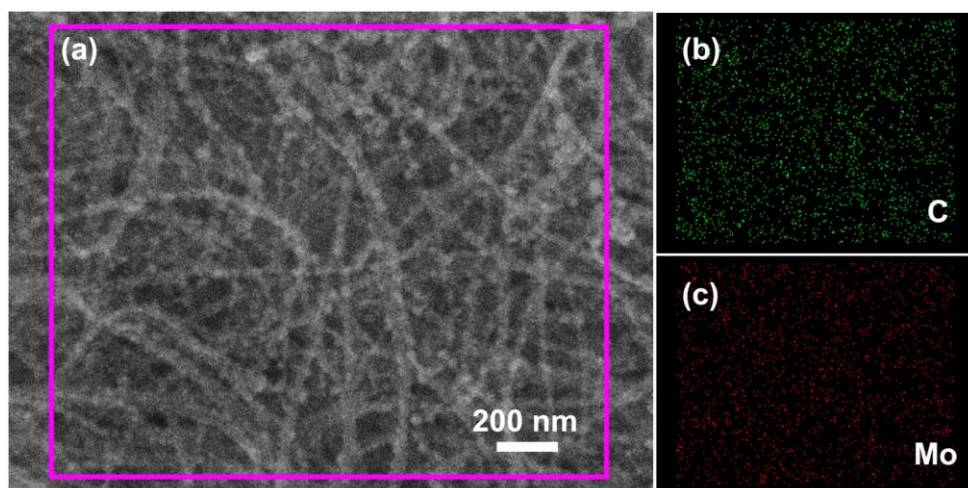


**Figure S6.** SEM image of CC@Mo<sub>2</sub>C NPs and corresponding EDS element mappings of (b) C and (c) Mo ascribed to the pink square area marked in (a), implying the even distribution of Mo<sub>2</sub>C nanoparticles on CNT cloth.

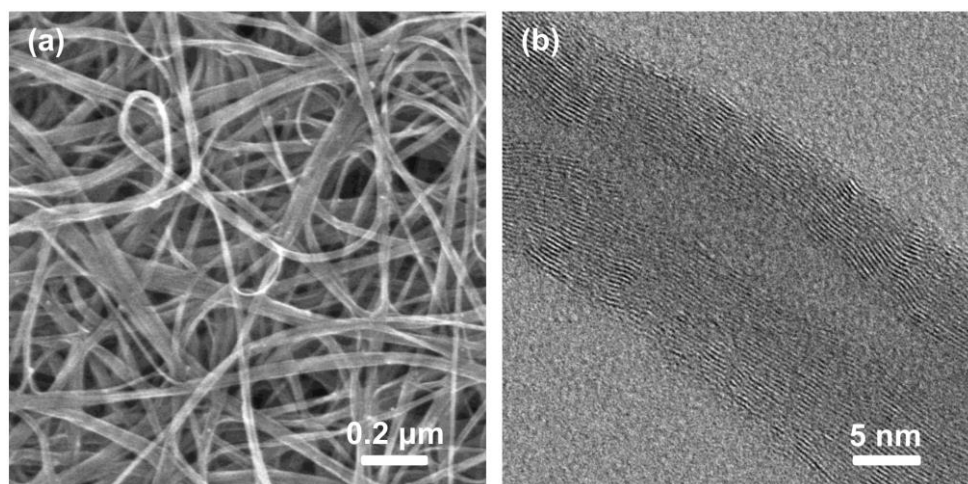


**Figure S7.** (a) SEM and (b) high-resolution TEM images of the pristine CNT cloth.

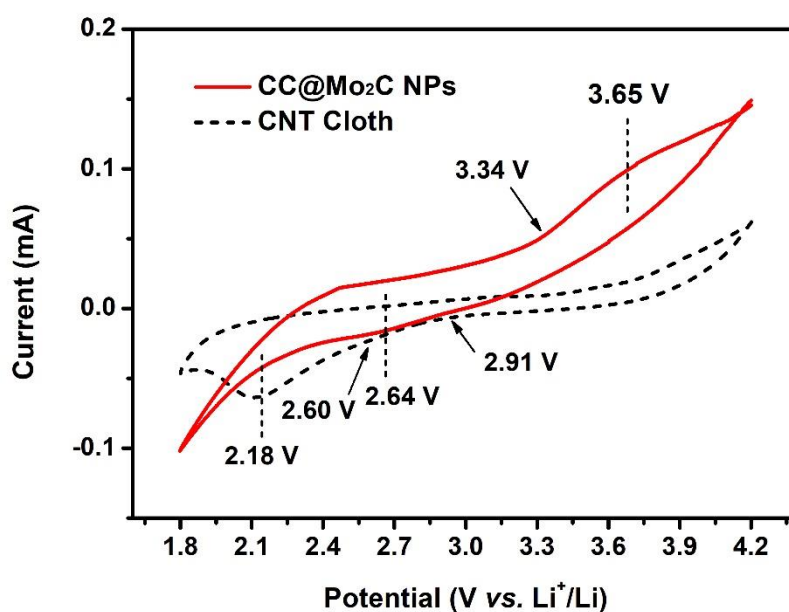


**Figure S8.** CV curves of **quasi-solid-state** Li-CO<sub>2</sub> cells with pristine CNT cloth or CC@Mo<sub>2</sub>C NPs cathodes under CO<sub>2</sub> at a scan rate of 0.1 mV s<sup>-1</sup> from 1.8 V to 4.2 V.

From these CV curves in Figure S8, it can recognize that the CO<sub>2</sub> reduction peaks were located at 2.64 V (starting from 2.91 V) for CC@Mo<sub>2</sub>C NPs and 2.18 V (starting from 2.60 V) for CNT cloth, respectively. During the anodic sweep, only CC@Mo<sub>2</sub>C NPs showed a broad CO<sub>2</sub> oxidation peak at 3.65 V, while no recognizable oxidation peak can be observed below 4.2 V in pure CNT cloth. Meanwhile, the area of CV curve of CC@Mo<sub>2</sub>C NPs was distinctly bigger than that of CNT cloth. The above phenomenon further gave a proof of the fact that this flexible and free-standing hybrid catalyst possessed a remarkably enhanced kinetics of both CO<sub>2</sub>RR and CO<sub>2</sub>ER, due to the employment of ultrafine Mo<sub>2</sub>C nanoparticles.

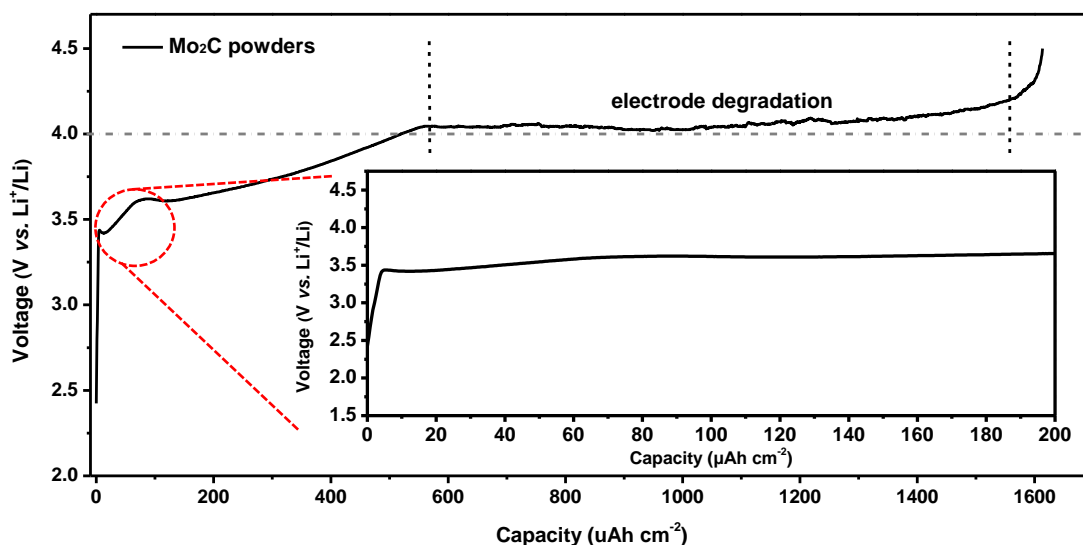


**Figure S9.** Galvanostatic charge profile of pure Mo<sub>2</sub>C powders in this quasi-solid-state system under CO<sub>2</sub> atmosphere at a current of 20 μA over the voltage window of 1.8-4.5 V.

On account of different relative stability of carbon and Mo<sub>2</sub>C-based catalysts in this special quasi-solid system, the electrochemical properties of Mo<sub>2</sub>C powders in CO<sub>2</sub> were investigated with the purpose of determining appropriate upper cut-off voltage. Two distinct charge processes have occurred in the above galvanostatic charge profile, in good accordance with the results of another Mo-based Li-CO<sub>2</sub> battery with liquid electrolyte reported previously.<sup>[S1]</sup> It is considered that the initial stage at 3.4-3.6 V should be originated from the decomposition of discharge product while the undesirable electrode degradation contributes to the long plateau above 4.0 V. Hence, the charge potential of CC@Mo<sub>2</sub>C NPs is stipulated below 4.0 V to make sure the electrode structure integrity.

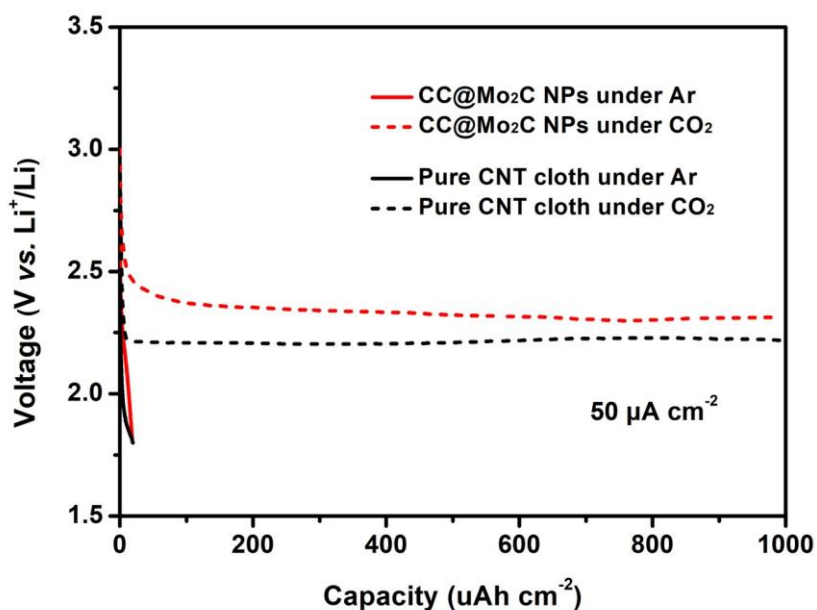


**Figure S10.** Galvanostatic discharge profiles of the quasi-solid-state Li-CO<sub>2</sub> cells with pristine CNT cloth or CC@Mo<sub>2</sub>C NPs cathodes at a current density of 50 uA cm<sup>-2</sup> under inert atmosphere of Ar.

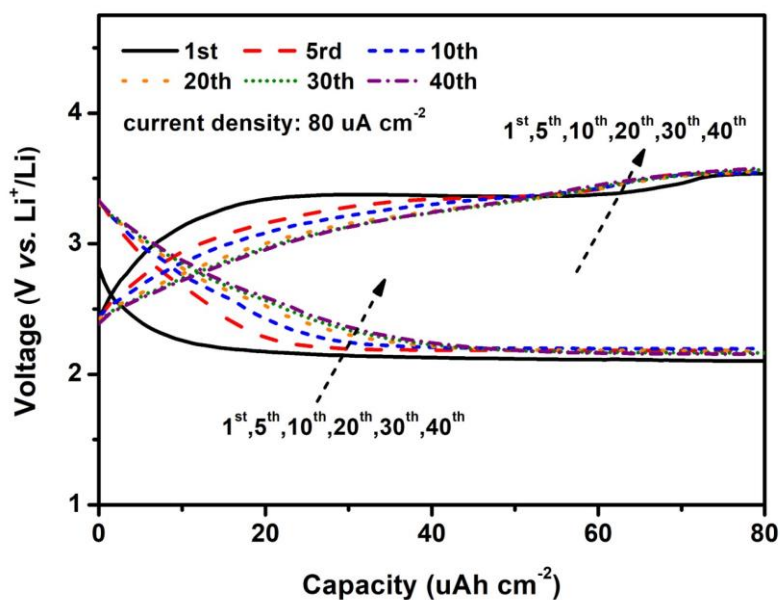


**Figure S11.** Cycling behavior of CC@Mo<sub>2</sub>C NPs electrode for the selected cycles under CO<sub>2</sub> at a current of 80 uA cm<sup>-2</sup> and curtailing capacity of 80 uAh cm<sup>-2</sup>.

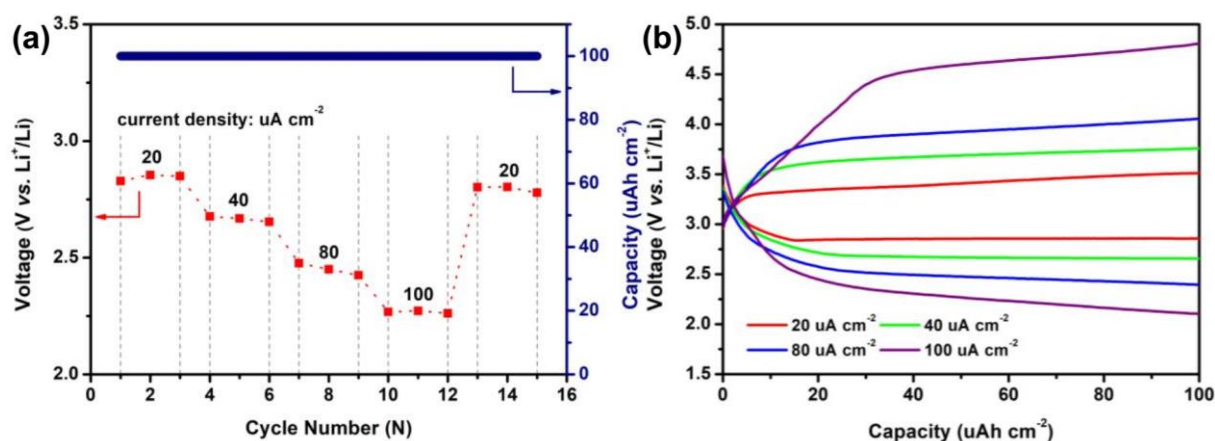


**Figure S12.** (a) Rate performance of CC@Mo<sub>2</sub>C NPs electrode at the current densities of 20, 40, 80 and 100  $\mu\text{A cm}^{-2}$  with the curtailing capacity of 100  $\mu\text{Ah cm}^{-2}$ . (b) Corresponding galvanostatic discharge/charge profiles of the CC@Mo<sub>2</sub>C NPs at different current densities.

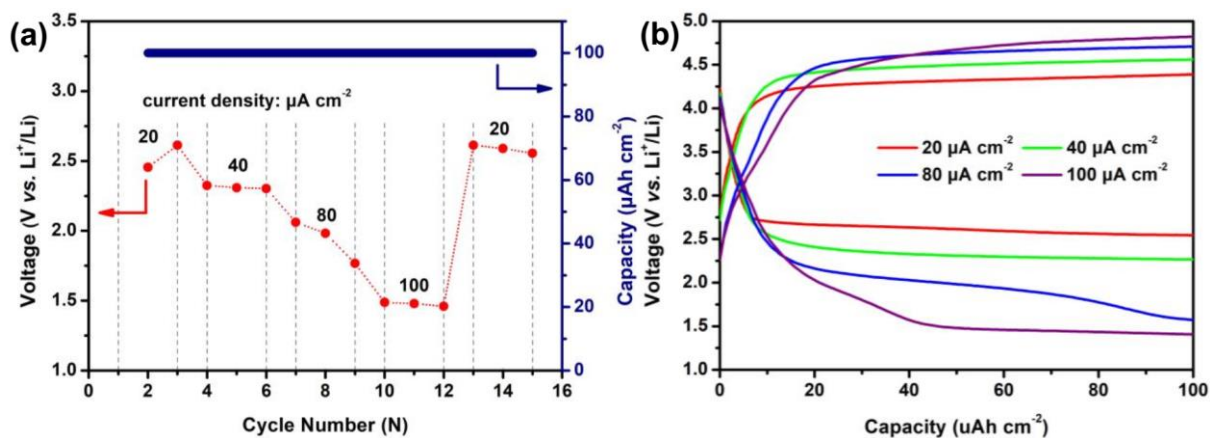


**Figure S13.** (a) Rate performance of pure CNT cloth electrode at the current densities of 20, 40, 80 and 100  $\mu\text{A cm}^{-2}$  with the curtailing capacity of 100  $\mu\text{Ah cm}^{-2}$ . (b) Corresponding galvanostatic discharge/charge profiles of pure CNT cloth at different current densities.

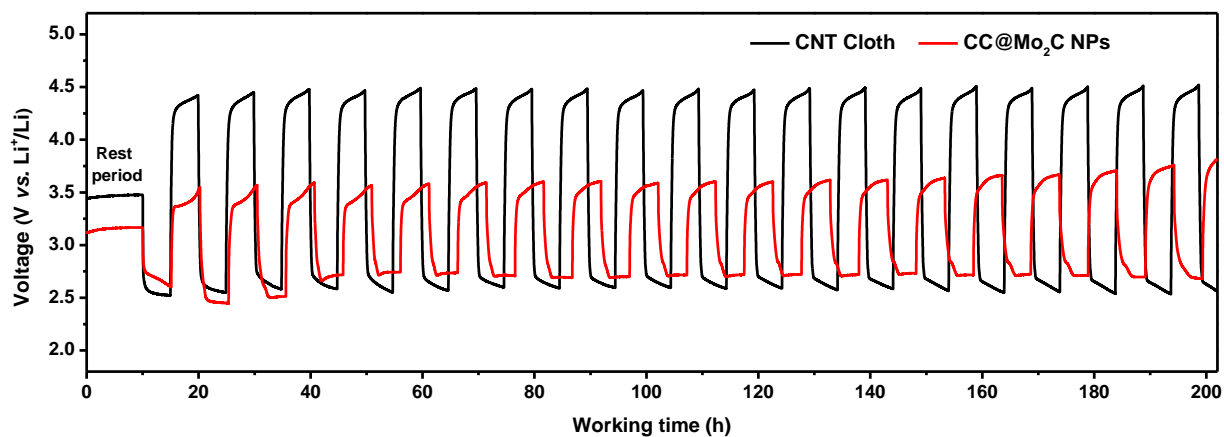


**Figure S14.** Voltage-time curves of the **quasi-solid-state** Li-CO<sub>2</sub> batteries with CNT cloth and CC@Mo<sub>2</sub>C NPs free-standing film as working electrodes at a current density of 20  $\mu\text{A cm}^{-2}$ , curtaining capacity of 100  $\mu\text{Ah cm}^{-2}$ .

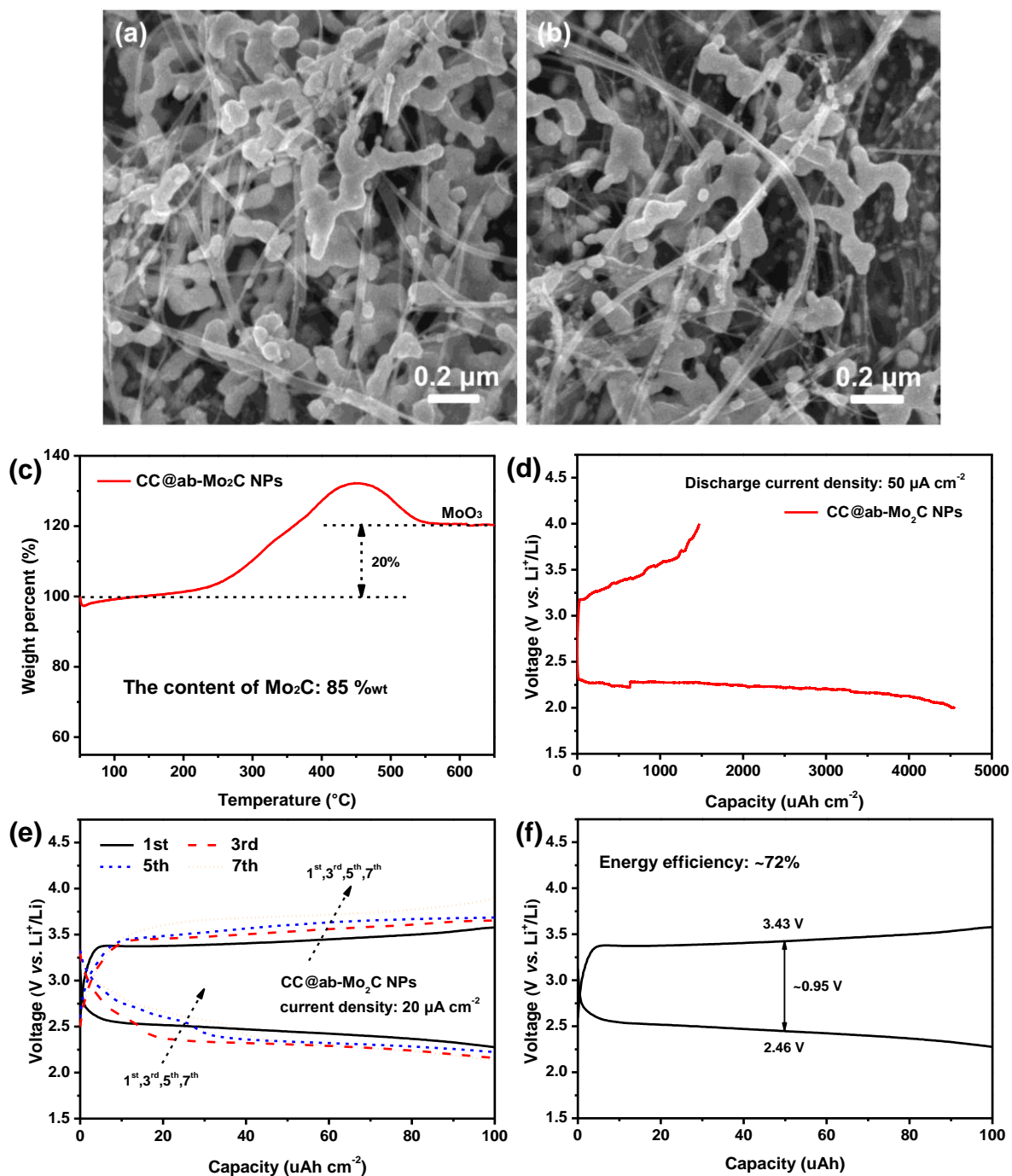


**Figure S15.** (a,b) Typical SEM images and (c) TG curve of the as-synthesized CC@ab-Mo<sub>2</sub>C NPs hybrid film. (d) Galvanostatic discharge/charge profiles of CC@ab-Mo<sub>2</sub>C NPs at 50 μA cm<sup>-2</sup>. (e) Cycling behaviours and (f) the discharge/charge profiles at the first cycle of CC@ab-Mo<sub>2</sub>C NPs at 20 μA cm<sup>-2</sup> and curtailing capacity of 100 μAh cm<sup>-2</sup>.

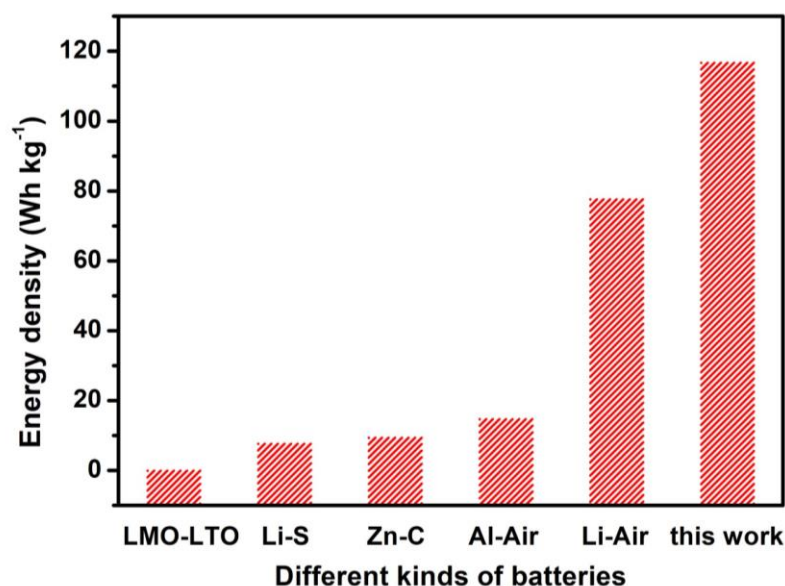


**Figure S16.** Comparison of the energy density based on the total weight of the device between several typical kinds of fiber-shaped novel batteries, including the LMO-LTO battery,<sup>[S2]</sup> Li-S battery,<sup>[S3]</sup> Zn-C battery,<sup>[S4]</sup> Al-air battery,<sup>[S5]</sup> Li-air battery<sup>[S6]</sup> and Li-CO<sub>2</sub> battery in this work. The results were obtained from the data which the literature provided, or by estimating based on the electrochemical performance and basic parameters of common experimental materials. LMO and LTO represent LiMn<sub>2</sub>O<sub>4</sub> and Li<sub>4</sub>Ti<sub>5</sub>O<sub>12</sub>, respectively.

**Table S1.** Comparisons between several typical kinds of novel fiber-shaped batteries.

	Cathode	Anode	State of electrolyte	Capacity (mAh cm <sup>-2</sup> ) Based on cathode	Energy density (Wh kg <sup>-1</sup> ) Based on device
This work	CC@Mo <sub>2</sub> C NPs sheet	Li wire	GPE	3.415	117
Li-ion battery <sup>[S2]</sup>	LiMn <sub>2</sub> O <sub>4</sub> @CNT fiber	Li <sub>4</sub> Ti <sub>5</sub> O <sub>12</sub> @CNT fiber	Liquid electrolyte	0.07	0.29
Li-S battery <sup>[S3]</sup>	S@CMK3@rGO @CNT fiber	Li wire	Liquid electrolyte	2.165	8
Zn-C battery <sup>[S4]</sup>	CNF@MnO <sub>2</sub> fiber	CNF@Zn powder fiber	Liquid electrolyte	1.85	9.75
Al-Air battery <sup>[S5]</sup>	CNT@Ag NPs sheet	Al spring	GPE	/	15
Li-Air battery <sup>[S6]</sup>	Aligned CNT sheet	Li wire	GPE	2.4	80

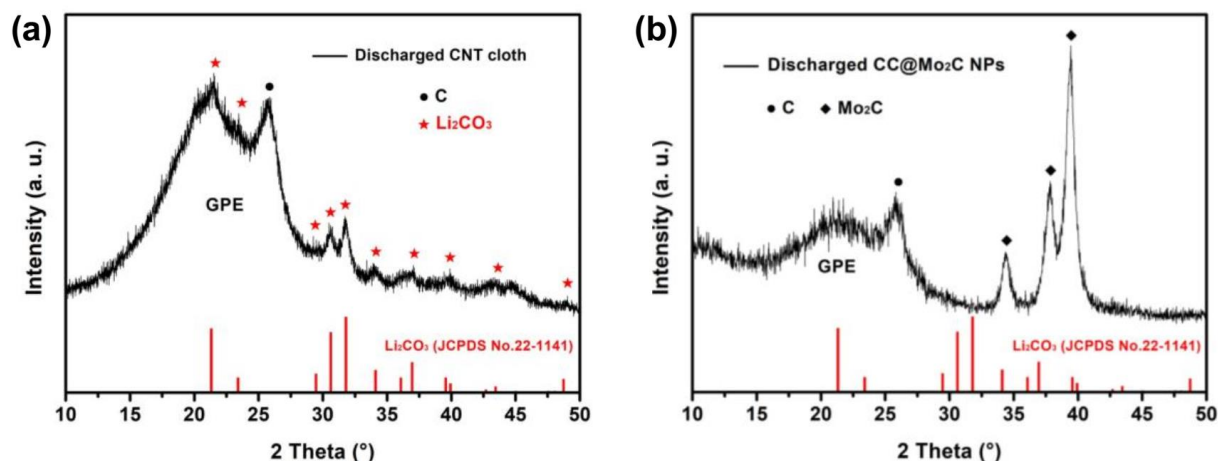


**Figure S17.** XRD patterns of (a) CNT cloth and (b) CC@Mo<sub>2</sub>C NPs electrodes after the first discharge process, which suggested that different discharge products were formed in these two Li-CO<sub>2</sub> batteries using different catalysts.

To reduce the influence of GPE on the XRD measurement for discharge products, we try our best to carefully eliminate the adherent GPE layer by hand in an Ar-filled glove box. Although the broad peak belonging to GPE can be still detected in the XRD patterns, the characteristic diffraction peaks of discharge products are strong enough to be observed.

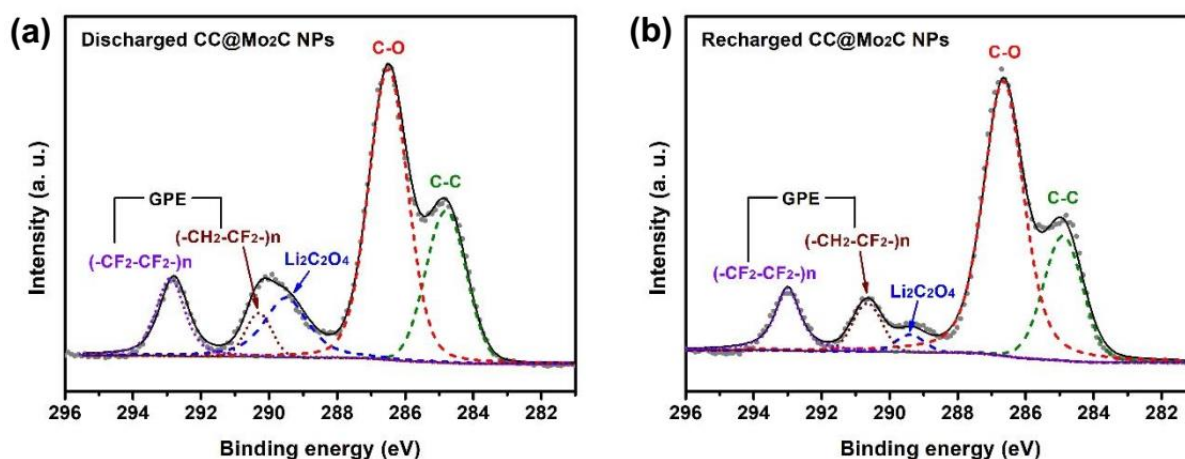


**Figure S18.** The high-resolution XPS spectra of C 1s for CC@Mo<sub>2</sub>C NPs electrode at (a) discharged state and (b) charged state.

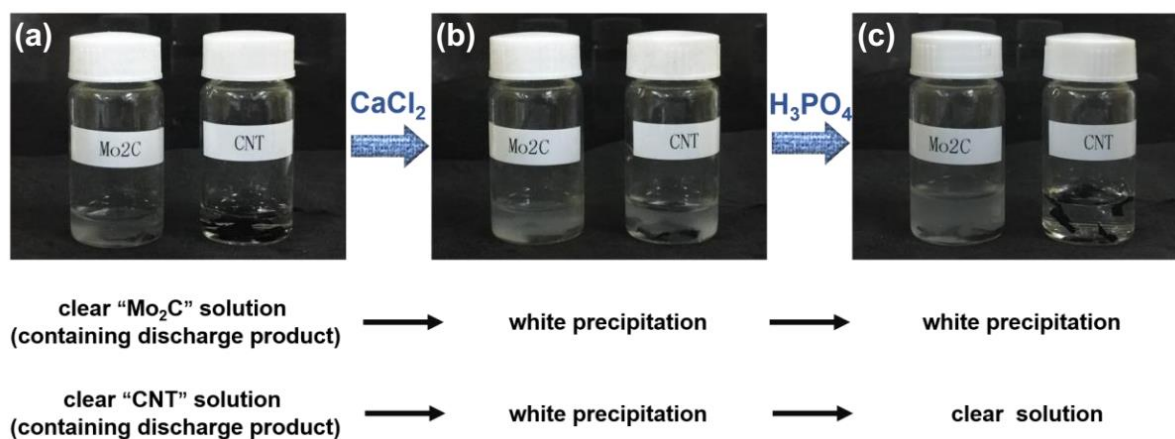


**Figure S19.** The photographs depicting two bottles of solution containing different discharge products of Mo<sub>2</sub>C and CNT, respectively, after (a) dissolving discharge product in oxygen-free distilled water, (b) adding a few drops of saturated CaCl<sub>2</sub> solution and (c) the following excessive addition of 1 Mol H<sub>3</sub>PO<sub>4</sub>.

Given that XRD measurement can not obtain its characteristic signals due to the amorphous property, we employed a special precipitation method to elucidate the existence of C<sub>2</sub>O<sub>4</sub><sup>2-</sup> in the discharge products of Mo<sub>2</sub>C. All of the following operations were conducted under the protection of Ar. The discharged pure Mo<sub>2</sub>C and CNT cathodes were transferred into two different glasses filled with equal amount of oxygen-free distilled water, respectively. After the dissolution of discharge products, a few drops of saturated CaCl<sub>2</sub> solution were added into them. It can be observed from Figure S19 that white precipitations both appeared at these two glasses. However, when enough 1 Mol H<sub>3</sub>PO<sub>4</sub> was mixed, only the suspension in "CNT" glass became pellucid while some precipitations in "Mo<sub>2</sub>C" glass remained. It proved that the latter white precipitation in "Mo<sub>2</sub>C" glass was not CaCO<sub>3</sub>. To our best knowledge, H<sub>2</sub>C<sub>2</sub>O<sub>4</sub> was the only stable acid consisting of only C, H and O elements of which the acidity is stronger than that of H<sub>3</sub>PO<sub>4</sub> at the same time. Therefore, this undissolved precipitation can be considered as CaC<sub>2</sub>O<sub>4</sub>. Based on these evidences, it is believable that the discharge product of Mo<sub>2</sub>C should contain C<sub>2</sub>O<sub>4</sub><sup>2-</sup>, thus promoting the possibility of the proposed mechanism.

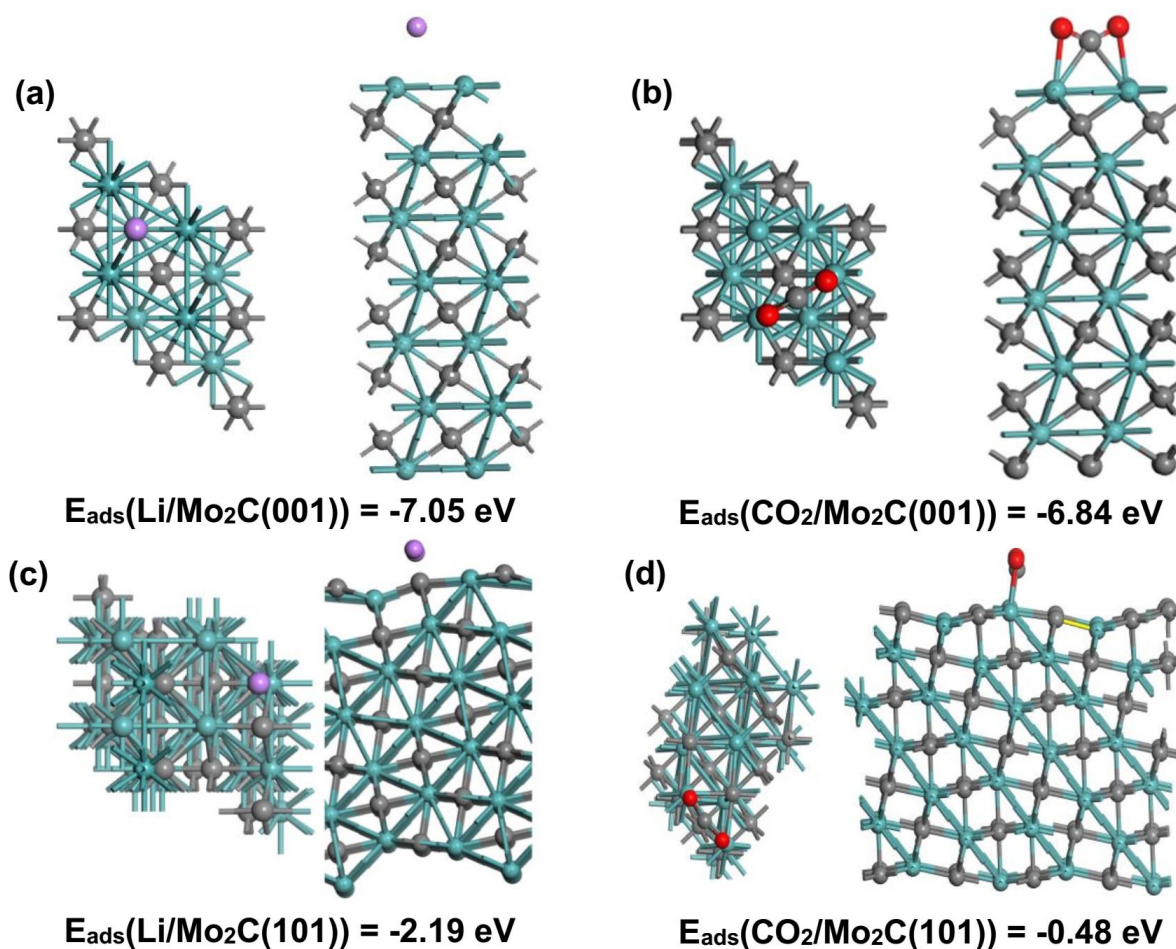


**Figure S20.** Top (left) and side (right) view of the optimized energetically most favorable structures of (a) Li and (b)  $\text{CO}_2$  adsorbed on  $\text{Mo}_2\text{C}$  (001) surface, (c) Li and (d)  $\text{CO}_2$  adsorbed on  $\text{Mo}_2\text{C}$  (101) surface. The cyan, purple, grey and red balls represent Mo, Li, C and O, respectively.

Given that (001) and (101) surfaces dominate the Wulff shape of  $\text{Mo}_2\text{C}$  nanoparticles,<sup>[S7]</sup> these two thermodynamically abundant Mo-terminated surfaces have been studied, with the models shown in Figure S20. Due to the relatively weak interaction of Li on  $\text{Mo}_2\text{C}$  (101) surface (-2.19 eV), only (001) surface is concentrated in the following simulations.

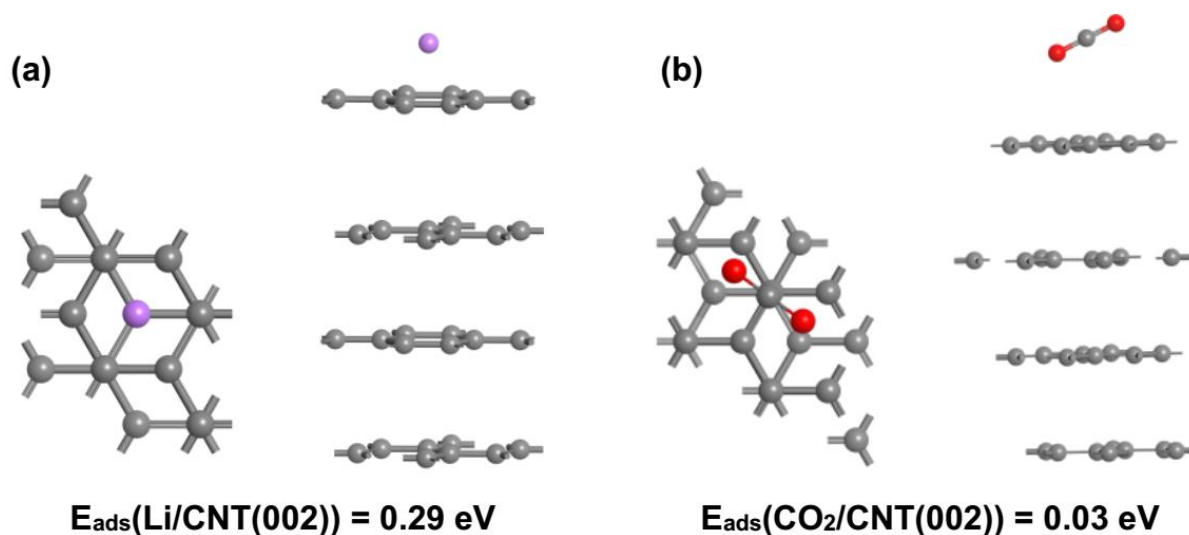


**Figure S21.** Top (left) and side (right) view of the optimized energetically most favorable structures of (a) Li and (b) CO<sub>2</sub> adsorbed on CNT (002) surface, respectively. The purple, grey and red balls represent Li, C and O, respectively.

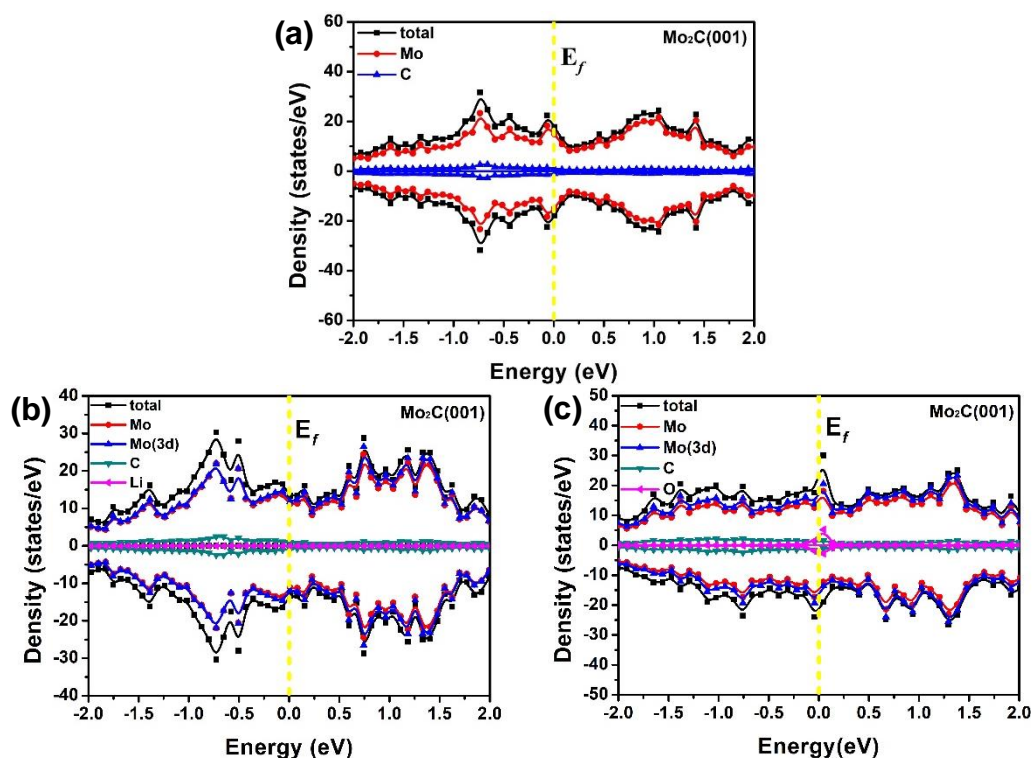


**Figure S22.** The electronic density of states (e-DOS) around the Fermi-level ( $E_f$ ) of Mo<sub>2</sub>C (001) surface at different stages: (a) pristine, (b) after the adsorption of one Li atom and (c) after the adsorption of one CO<sub>2</sub> molecule.

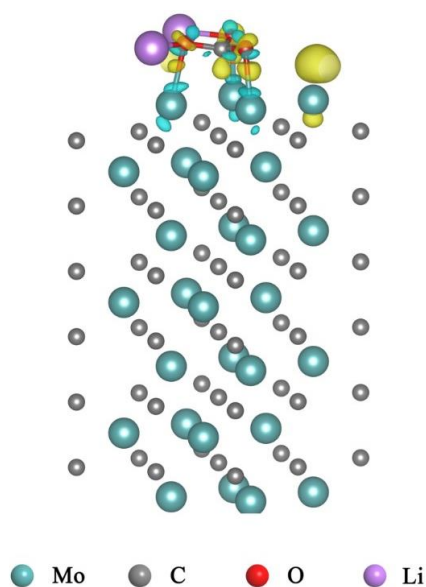


**Figure S23.** Charge density difference of  $\text{Li}_2\text{CO}_3$  molecule adsorbed on  $\text{Mo}_2\text{C}$  (001) surface. The cyan, purple, grey and red balls represent Mo, Li, C and O, respectively. The yellow and light blue regions represent the charge accumulation and charge loss, respectively.

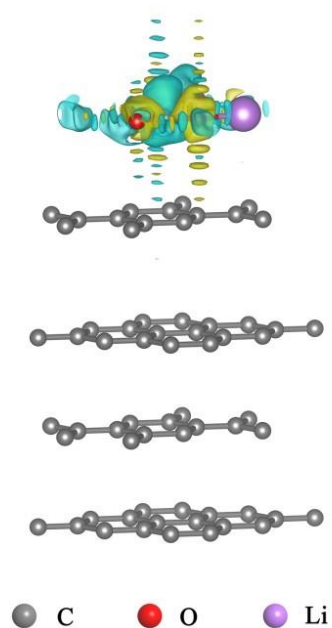


**Figure S24.** Charge density difference of  $\text{Li}_2\text{CO}_3$  adsorbed on CNT (002) surface, depicting the weak electrons transfer between  $\text{Li}_2\text{CO}_3$  and CNT. The purple, grey and red balls represent Li, C and O, respectively. The yellow and light blue regions represent the charge accumulation and charge loss, respectively.

## References

- [S1] Y. Hou, J. Wang, L. Liu, Y. Liu, S. Chou, D. Shi, H. Liu, Y. Wu, W. Zhang and J. Chen, *Adv. Funct. Mater.* **2017**, *27*, 1700564.
- [S2] J. Ren, Y. Zhang, W. Bai, X. Chen, Z. Zhang, X. Fang, W. Weng, Y. Wang and H. Peng, *Angew. Chem., Int. Ed.* **2014**, *53*, 7864.
- [S3] X. Fang, W. Weng, J. Ren and Huisheng Peng, *Adv. Mater.* **2016**, *28*, 491.
- [S4] X. Yu, Y. Fu, X. Cai, H. Kafafy, H. Wu, M. Peng, S. Hou, Z. Lv, S. Ye and D. Zou, *Nano Energy* **2013**, *2*, 1242.
- [S5] Y. Xu, Y. Zhao, J. Ren, Y. Zhang and Huisheng Peng, *Angew. Chem., Int. Ed.* **2016**, *55*, 7979.
- [S6] Y. Zhang, L. Wang, Z. Guo, Y. Xu, Y. Wang and H. Peng, *Angew. Chem., Int. Ed.* **2016**, *55*, 4487.
- [S7] R. Kannan, U. Bipinlal, S. Kurungot and V. K. Pillai, *Phys. Chem. Chem. Phys.* **2011**, *13*, 10312.